KINEMATICS AND STELLAR POPULATION STUDIES OF THE GALACTIC BULGE

MAJOR RESEARCH PROJECT

Conducted at Leiden Observatory

Under the supervision of Koenraad Kuijken and Mario Soto

Tri Laksmana Astraatmadja
Student Number 0646385
astraatmadja@strw.leidenuniv.nl

Abstract

We report the photometry and kinematical analysis of stars in a $2.5' \times 2.5'$ field centered at $(l, b) = (9.86°, \ -7.61°)$ in a direction toward the Galactic bulge, as part of a larger project to obtain 3-D kinematics of stars in the Galactic bulge. The images were taken by the *Hubble Space Telescope* Wide Field Planetary Camera 2 (WFPC2) in the F606W and F814W bands. The resulting photometric catalogue is compared with a proper motions catalogue of stars in the same field.

Proper motions measurements were made by assuming that the average motion of stars in the field are zero. However, because the field is located ~ 4 arc minutes away from the center of the globular cluster NGC 6656, residual motions from this cluster are still present in the proper motions measurements. A technique is devised to remove this residual to obtain more accurate proper motion measurements. Bulge/disk decomposition is performed by fitting the velocity distribution with a bivariate bimodal Gaussian function. The resulting l and b velocity dispersions for bulge stars are 85 and 109 km s^{-1}, respectively.

Compared with previous proper motions measurements of stars in Baade's Window that centered on $(l, b) = (1.13°, -3.76°)$, the kinematics in our field is considerably colder than that of Baade's Window. However, our field is located farther West of the Galactic Center and numerous findings show that l velocity dispersions is a function of Galactic longitude l: it peaks at $l = 0$ and decreases toward positive and negative l. This function is one of the signatures that the bulge is rotating as a solid body, and our kinematic studies conform to this idea.

Key words: Astrometry – Catalogues – Galaxy: bulge – Galaxy: globular clusters: individual: NGC 6656 – Galaxy: kinematics and dynamics – Stars: kinematics.

Abstrak Bahasa Indonesia

Sebagai bagian dari proyek yang lebih besar untuk menentukan kinematika tiga dimensi bintang-bintang di tonjolan pusat Galaksi, kami melaporkan hasil fotometri dan analisis kinematika bintang-bintang di sebuah medan berukuran $2.5' \times 2.5'$ yang berpusat di $(l, b) = (9.86°,\ -7.61°)$. Medan ini berada dalam arah menuju tonjolan pusat Galaksi. Citra diambil pada pita F606W dan F814W dengan menggunakan *Wide Field Planetary Camera* 2 (WFPC2) yang terpasang pada Teleskop Ruang Angkasa Hubble. Katalog fotometri yang dihasilkan kemudian dicocokkan dengan katalog gerak diri bintang-bintang pada medan yang sama.

Gerak diri bintang diukur dengan mengasumsikan gerakan rata-rata bintang-bintang di medan tersebut sama dengan nol. Namun karena medan ini terletak ~ 4 menit busur dari pusat gugus bola NGC 6656, residu gerak diri masih tersisa dalam hasil pengukuran gerak diri. Sebuah teknik khusus harus dikembangkan agar residu ini dapat dihilangkan dan dengan demikian dapat dihasilkan pengukuran gerak diri yang lebih akurat. Dekomposisi tonjolan/cakram Galaksi dilakukan dengan melakukan pengepasan kurva pada distributi gerak diri dengan fungsi Gauss bivariat berpuncak ganda. Dari pengepasan kurva ini diperoleh dispersi kecepatan bintang-bintang tonjolan pusat dalam arah l dan b masing-masing adalah 85 dan 109 km s^{-1}.

Apabila dibandingkan dengan pengukuran sebelumnya dalam arah Jendela Baade yang berpusat pada $(l, b) = (1.13°, -3.76°)$, kinematika bintang-bintang pada medan ini jelas lebih dingin daripada yang terukur di Jendela Baade. Namun, medan ini terletak lebih ke arah barat dari pusat Galaksi dan telah banyak temuan yang menunjukkan bahwa dispersi kecepatan merupakan fungsi dari l: Berpuncak pada arah $l = 0$ dan menurun ke arah l positif dan negatif. Fungsi ini merupakan tanda bahwa tonjolan pusat berrotasi sebagai benda padat, dan hasil-hasil dalam pekerjaan ini menyetujui ide ini.

Kata kunci: Astrometri – Katalog – Bima Sakti: tonjolan pusat – Bima Sakti: gugus bola: individual: NGC 6656 – Bima Sakti: kinematika dan dinamika – Bintang: kinematika.

Nederlandse Samenvatting

Wij maken verslag van de fotometrie en kinematische analyse van sterren in een $2.5' \times 2.5'$ veld met middelpunt $(l, b) = (9.86°, \ -7.61°)$, in de richting van de centrale verdikking van de Melkweg, als deel van een groter project om de driedimensionale kinematica van de sterren in de verdikking te verkrijgen. De beelden werden gemaakt door de Wide Field Planetary Camera 2 (WFPC2) van de *Ruimtetelescoop Hubble* in de F606W en F814W band. De resulterende fotometrische catalogus wordt dan vergeleken met een eigenbewegingscatalogus van de sterren in hetzelfde veld.

Eigenbewegingsmetingen waren gemaakt door annemen te maken dat de gemiddeldebeweging van alle sterren in de veld zijn null. Maar, omdat het veld op een afstand van ~ 4 boogminuten van het centrum van de sterrenhoop NGC 6656 staat, zijn er nog resterende bewegingen van de hoop aanwezig. Wij bedenken een techniek om dit residu te verwijderen. Als resultaat verkrijgen wij meer nauwkeurige metingen van de eigenbewegingen. De verdikking-en-schijfpopulatie wordt ontbonden door de snelheidsdistributie aan een bimodale Gaussfunctie te fitten. De resulterende l en b snelheidsdispersies van de sterren uit de verdikking zijn respectievelijk 85 en 109 km s^{-1}.

Vergeleken met vorige eigenbewegingsmetingen van sterren in de richting van *Baade's Window* met middelpunt $(l, b) = (1.13°, -3.76°)$, is de kinematica van dit veld aanzienlijk kouder dan die uit *Baade's Window*. Echter onze veld ligt verder ten westen van het Galactische centrum en vorige ontdekkingen laten zien dat de snelheidsdispersie is een functie van Galactische lengte l: het piekt op $l = 0$ en afneemt bij kleinere of grotere waardes van l. Deze functie is een van tekenen dat de verdikking roteert als een vast licham, en onze metingen dragen bij deze idee.

Sleutelwoorden: Astrometrie – Catalogus – Melkweg: centrale verdikking – Melkweg: sterrenhoop: individueel: NGC 6656 – Melkweg: kinematica en dynamica – Sterren: kinematica.

Résumé Français

Le travail présenté ici fait partie d'un projet plus vaste dont le but est d'obtenir une description cinématique du bulbe galactique. Nous présentons la photométrie et l'analyse cinématique d'étoiles dans un champ de $2.5' \times 2.5'$ centré à $(l, b) = (9.86°, \ -7.61°)$, en direction du bulbe Galactique. Les images que nous utilisons ont été prises par le Wide Field Planetary Camera 2 (WFPC2) du Télescope spatial Hubble, dans les bandes F606W et F814W. Le catalogue de mesures photométriques est ensuite comparé avec un catalogue des mouvements propre d'étoiles du même champ.

Les mesures des mouvement propre sont réalisées en faisent l'hypothése d'un mouvement moyen d'étoiles du champ nul. Mais le champ est situé à environ 4 minutes d'arc du centre de l'amas globulaire NGC 6656, et ceci induit des mouvements résiduels dans la mesure de mouvements propres. Nous avons développé une technique pour compenser cet effet et obtenir des mesures du mouvement propre plus précises. La décomposition bulbe/disque est obtenue par l'ajustement de la distribution des vitesses avec une fonction Gaussienne bimodale. Les dispersions des vitesses dans les directions l et b sont de 85 et 109 km s^{-1} respectivement.

Nous avons comparé la cinématique de notre champ avec celle de la Fenêtre de Baade que centré à $(l, b) = (1.13°, -3.76°)$. Celle que nous mesurons est considérablement plus froide. Pourtant, notre champ situé plus à l'ouest du centre Galactique et un nombre de mesures montre que de la dispersion de vitesses du bulbe galactique est en fonction de l: elle est maximale autour de $l = 0$ et diminue vers l positif et négatif. Cette fonction est une des nombreuses indications que le bulbe galactique tourne comme un solide, et notre étude cinématique se conforme à cette idée.

Mots-clés: Astrométrie – Catalogue – La Galaxie: bulbe – La Galaxie: Amas globulaire: individuel: NGC 6656 – La Galaxie: cinématique et dynamique – Etoile: cinématique

Contents

List of Tables

List of Figures

Chapter 1

Introduction

1.1 Dissecting the Milky Way

Like an anatomist inspecting a *corpus*, our Milky Way can be dissected and its different parts inspected to figure out its working mechanism in more detail. After an understanding of each body part is obtained, all facts are then combined and connected with each other in order to obtain the bigger and general picture of how the *corpus* works as a whole.

It is with this idea in mind is how the study of galactic structure is sometimes done. The Milky Way is an important sample for somebody who wants to undertake the gigantic task of studying the structure of galaxies: we are inside it and we can study the Galaxy in resolutions unsurpassed by studies of extragalaxies. However, dissecting the Milky Way is no easy matter because distinguishing different components might not as easy as distinguishing components in a human body. In fact, it took us a long time before we even realise that the Milky Way is a stellar system. The "discovery" of our Milky Way as a stellar system is a long and painful process. After William Herschel's (1785) attempt to understand the Milky Way's structure by "star gauging", Jacobus Kapteyn attacked the same problem by using massive amount of proper motion data and pioneering international collaborations through his plan of selected areas (Kapteyn, 1922), culminating in the Kapteyn Universe, in which the universe is lenticular in shape with a radius of approximately 5 kpc and the Sun is slightly off-center. This was unfortunately incorrect due to ignorance to the absorption effect by interstellar medium.

Harlow Shapley's investigation of the distribution of globular clusters in the Milky Way (Shapley, 1918a,b, 1919a,b, Shapley and Shapley, 1919) led to a model contradicting the Kapteyn Universe. In his model the Milky Way is disc-shaped with the Sun on its plane but very much off-center at a distance of some 15 kpc from the center the disc. Shapley estimated the diameter of the Milky Way to be close to 100 kpc, an extremely large distance at that time and even almost 10 times larger than the Kapteyn universe. This enormous size compelled Shapley to conclude that the Milky Way comprises the whole universe. Later in 1920, these two model was then publicly presented by Harlow Shapley, championing his own model, and Heber Curtis, who supported the Kapteyn Universe model, in a public debate known since then as the Great Debate. In short time, Edwin Hubble will later resolve the question by using Cepheid to determine the distance to M31 (Hubble, 1922), once and for all showing that the Andromeda Nebula is not a member of the Milky Way but a sovereign system comparable to the Milky Way.

Although Shapley was wrong in supposing that the whole the universe comprised solely of the Milky Way while the numerous nebulae are members of the Milky Way, his model on the extent of the Milky Way and the Sun's position within it is basically correct although his estimates on the scale is much larger (modern estimate put the Sun at approximately 8 kpc from the center and the diameter of the Milky Way to be 30 kpc). Bertil Lindblad later developed a kinematic model of the Milky Way (Lindblad, 1927), which was developed into a more complete theory of Galactic stellar kinematics by Jan Oort (1927, 1928)

Once we understand the nature of spiral nebulae which are independent systems similar to our own, these pioneering works then serve as foundations for later works in galactic structure. Radio observations in 21 cm line (e.g. Oort et al. (1958)) provide a great advance in this field and play a major role in delineating the spiral structure of the Milky Way as well as other galaxies. The traditional work of large scale optical survey on all hemisphere of the sky also provided enormous amount of data for quantitative measurement of light distribution in the Milky Way as well as other galaxies. Based upon the light distribution we can divide galaxies into distinct components, the most prominent being the bulge and the disc (in some cases we can identify other components such as bars, lens, and ring components).

Thus our progress on this "cosmic anatomy" has allowed us to define various components (that can be or can not be) in a galaxy and providing us with a chance to explain their properties in more details, how they came to be that way and how will they evolve. Of course sharp boundaries between components are not always clear and it is hard to decompose two of more components, but attempts are constantly made and the scalpel of decomposition gets sharper as more reliable data pours in.

Eventually the study of the various components in our Galaxy, the Milky Way, leads to the big picture that ask two questions: First, what kind of galaxy the Milky Way is. Where does it stand on the classification scheme and what are its properties? Second, how did galaxies formed and how do they evolve? In order to answer the second question it is then necessary to compile the various high-resolution observation and measurements of the Milky Way's components and look for various clues that can contribute to the question.

1.2 The Galactic bulge

Early research in galactic structure mentions only the 'halo', 'nucleus' and 'disc' to indicate different parts of our Galaxy (Wyse et al., 1997). When Stebbins and Whitford (1947) detected the Galactic bulge for the first time, it was only mentioned as the "nucleus of our Galaxy." Bulges are later defined to be any allocation of "non-disk" light distribution of any galaxy that has a "disk." The resulting quantity is the disc-to-bulge ratio (D/B). The size of the bulge along with the size and morphology of the spiral arms later play a central role in galaxy classification (e.g Sandage and Bedke (1994)), which is so successful it implies a certain correctness in our understanding of galactic structure: Bulges are a defining component that underlie the Hubble sequence of galaxy classification, which then tells us something of a given galaxy's formation and evolution. However, early theoretical works on galaxy formation, for example Eggen et al. (1962) and Searle and Zinn (1978), discussed only the disc and the halo but not the bulge. This ignorance of the importance of bulges is understandable if we look at the optical map of the Galaxy (Figure 1.1) which does not clearly show any separate components toward the Galactic Center, since the area is heavily obscured by interstellar matter. However, the near-infrared map of whole sky clearly reveals the shape of bulge and its boundaries by their light-distribution.

This is thus the reason why we do care about bulges: understanding the morphology and evolution of bulges is part of answering the question of how galaxies form and evolve. In other words, an understanding of the parameters and processes that determine the disc-to-bulge ratio is part of the effort to understand the origin of the Hubble sequence as well as contribute to our understanding of galaxy formation.

The bulge of our Galaxy is the nearest bulge to us and the reason to study it is obviously because it permits high-resolution study of bulges. Despite this privileged position, there are still standing questions about our own Bulge. This problem comes from complications that appears if one tries to observe the Galactic Bulge. First and foremost, the interstellar matter (ISM) absorption toward the Galactic Centre can reach up to $A_V \sim 30$ mag (Binney and Merrifield, 1998), thus it limits optical observations to only small "windows" that have low and relatively

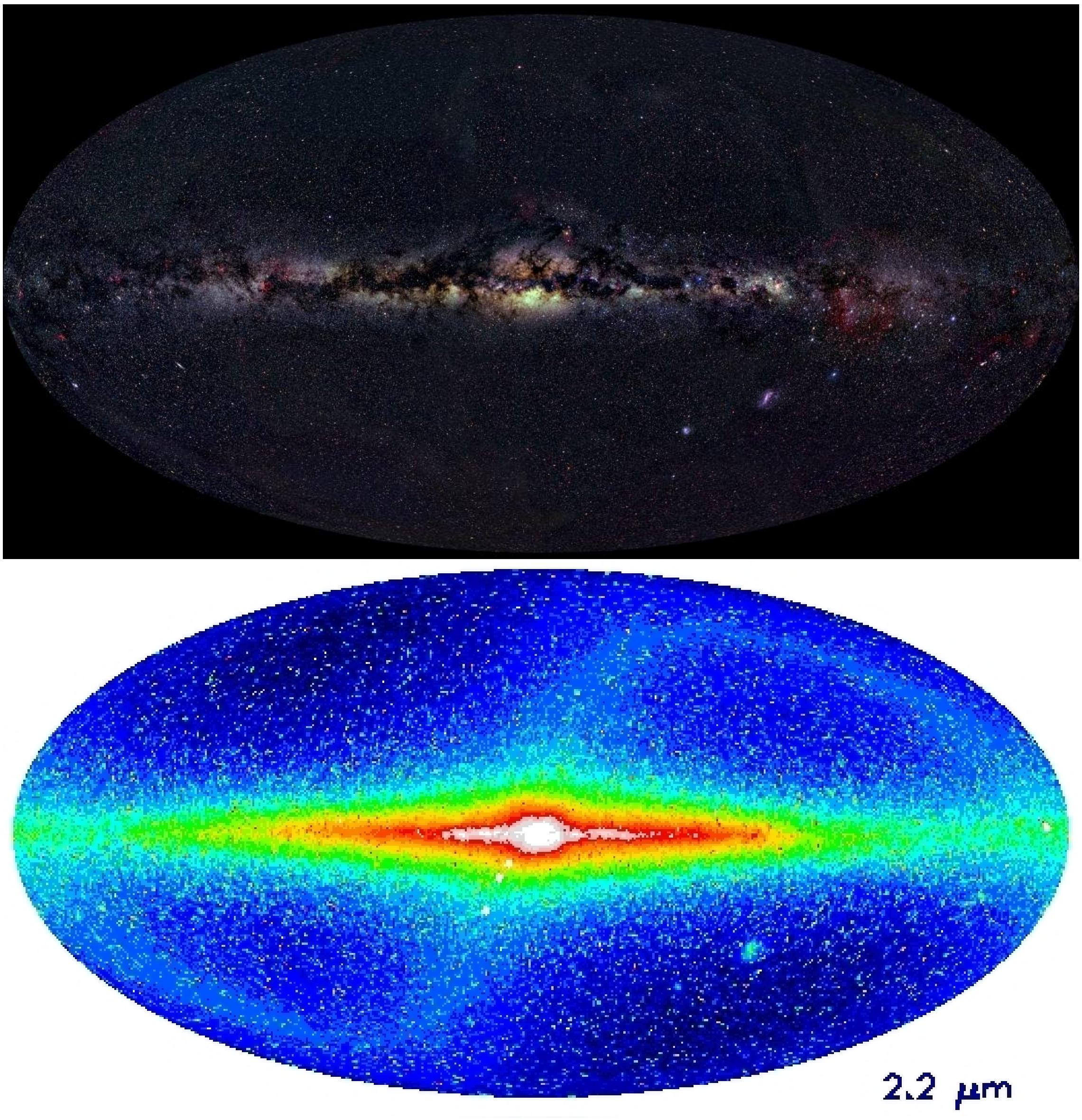

Figure 1.1: Top: An all-sky map of the Milky Way in optical wavelength (Copyright Axel Mellinger 2000). **Bottom:** The COBE-DIRBE all-sky map of the Milky Way in Near-IR (Dwek et al., 1995). The ISM obscuration of the Galactic Center makes the bulge can not be easily recognised. However, near-infrared maps reveals the shape and boundaries of the bulge.

uniform extinction like, for example, Baade's Window. These "windows" do not make life easier either as all objects sampled in a line of sight to these windows are a mixture of different populations. Exponential models for the disk predict that at least $\sim 50\%$ of the stars along the line of sight to Baade's Window are actually disk stars and not bulge stars (Kuijken and Rich, 2002). Without any information of their distance it would be difficult to separate bulge stars with disk stars. Near the turnoff point, bulge and disk stars overlap in colour (Holtzman et al., 1998), and this contamination further complicate our effort to discern the two group of stars.

In this project we are concentrating on obtaining the kinematics of the Galactic Bulge. The first such effort was conducted by Spaenhauer et al. (1992) who used Walter Baade's old plates as first epoch data. The plates were taken in 1950 and 1983 using the 200 inch Palomar telescope. With these data they measured the proper motions of bulge stars along Baade's Window and discussed the basic methods and problems that will later be a recurring theme in this field of study, namely contamination by disc population. Zhao et al. (1994) later use the same subset of data and complemented it with radial velocity and metallicity data taken by Rich (1988, 1990), and calculated the vertex deviation of the velocity ellipsoid, which is a signature of bulge triaxiality.

Various research had used radial velocity measurements to show that the bulge is rotating with peak velocity ~ 75 km s^{-1} (e.g. Minniti et al. (1992), Ibata and Gilmore (1995), Rich et al. (2007)) and has a large velocity dispersion that decreases as the Galactocentric distance gets larger. Since the proper motions measurements by Spaenhauer et al. (1992), other investigators such as Kuijken and Rich (2002) and Soto et al. (2007) have revisited the bulge and conducted more accurate measurements of the proper motion. The kinematics of the bulge puts it somewhere between purely rotating system like the disc and hot, non-rotating system like the halo (Minniti and Zoccali, 2008). A complete three-dimensional kinematics of bulge stars would be necessary if we want to obtain their orbits. This is important if we want do distinguish between the bulge and the inner disc stars.

Our project is part of the larger ongoing effort to obtain 3-D kinematics of bulge stars. It use images of selected fields toward the bulge that are available from the HST data archive. The archive has been available for more than a decade and contains enormous amount of WFPC2 images taken during the nineties. Second epoch images of these fields has been taken with the ACS (Advanced Camera for Survey) on board the HST, and results has been reported in Kuijken and Rich (2002), Kuijken (2004) and Soto et al. (2007). The selected fields and the progress of the project as a whole is shown in Figure 1.2. Radial velocity measurements by the VLT

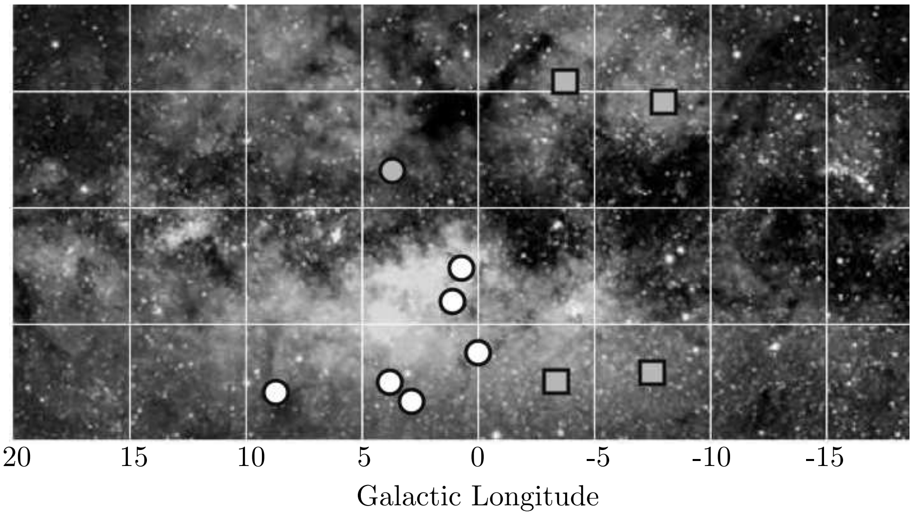

Figure 1.2: The fields on the project, superimposed on an optical map of the Galactic Bulge. White circles are fields for which proper motion and radial velocity measurements have been completed. The grey circle is a field initially considered but was discarded later, and grey squares are fields which measurements have not been completed.

VIMOS IFU also complement the proper motion data.

In this project we will report the photometric measurements of one particular field (Field 183635-235701) and the procedure to correlate the resulting photometric catalogue with the proper motion catalogue that has been previously measured. We will also describe the techniques and procedure to remove the systematic residual still present in the proper motions, as well as the technique to separate the disk and bulge populations. The next chapter will discuss the observations to obtain photometric data and the procedure to measure the magnitudes of each detected object. Techniques of crowded-field photometry will be described as well as the transformation to standard magnitudes. Chapter 3 will give an introduction on how to conduct proper motion measurements and the procedure for residual removals. We will also describe the assumption and methods in bulge/disk decomposition. The last chapter will discuss and conclude the results.

Chapter 2

Observations, measurements and calibration

2.1 The observations

Field 183635-235701 [$(\alpha, \delta) = 18^{\mathrm{h}}36^{\mathrm{m}}35^{\mathrm{s}}, -23^{\circ}57'01''$, $(l, b) = 9.87^{\circ}, -7.61^{\circ}$] is located ≈ 3.7 arcminutes from the center of the globular cluster NGC 6656 [$(\alpha, \delta) = 18^{\mathrm{h}}36^{\mathrm{m}}24.21^{\mathrm{s}}, -23^{\circ}54'12''$, $(l, b) = 9.89^{\circ}, -7.55^{\circ}$]. The observations were conducted on the 30th of September 1995 with the Wide Field Planetary Camera 2 (WFPC2), a wide-field imaging instrument on board the Hubble Space Telescope (HST). WFPC2 contains four identical Loral CCD chips, 800×800 pixels each. One chip, named the Planetary Camera 1 (PC1), has a 34" × 34" field-of-view with plate scale 0.045" per pixel, while the other three chips comprise the Wide Field Camera (WFC) each with 150" × 150" field-of-view and image scale of 0.1" per pixel. The three chips are arranged in an L-shaped field-of-view and are named WF2, WF3, and WF4 respectively. The images were made through the F606W and F814W filters (equivalent to wide V and I in the UBV system, respectively. For details about the filters, see Table 2.1). The field was imaged in 4 exposures of 1100 s each for F606W and 4 exposures of 1200 s each for F814W.

The orientation of the field with respect to the cluster is shown in Figure 2.1 while the HST image of the field itself is shown in Figure 2.2. We can see from Figure 2.1 that the edge of the cluster is close to the Wide-Field Camera 3 (WF3) and Wide-Field Camera 4 (WF4). Thus we can assume that some part of the stars in the field are members of the cluster, while some are field stars in the bulge or might even be disc stars.

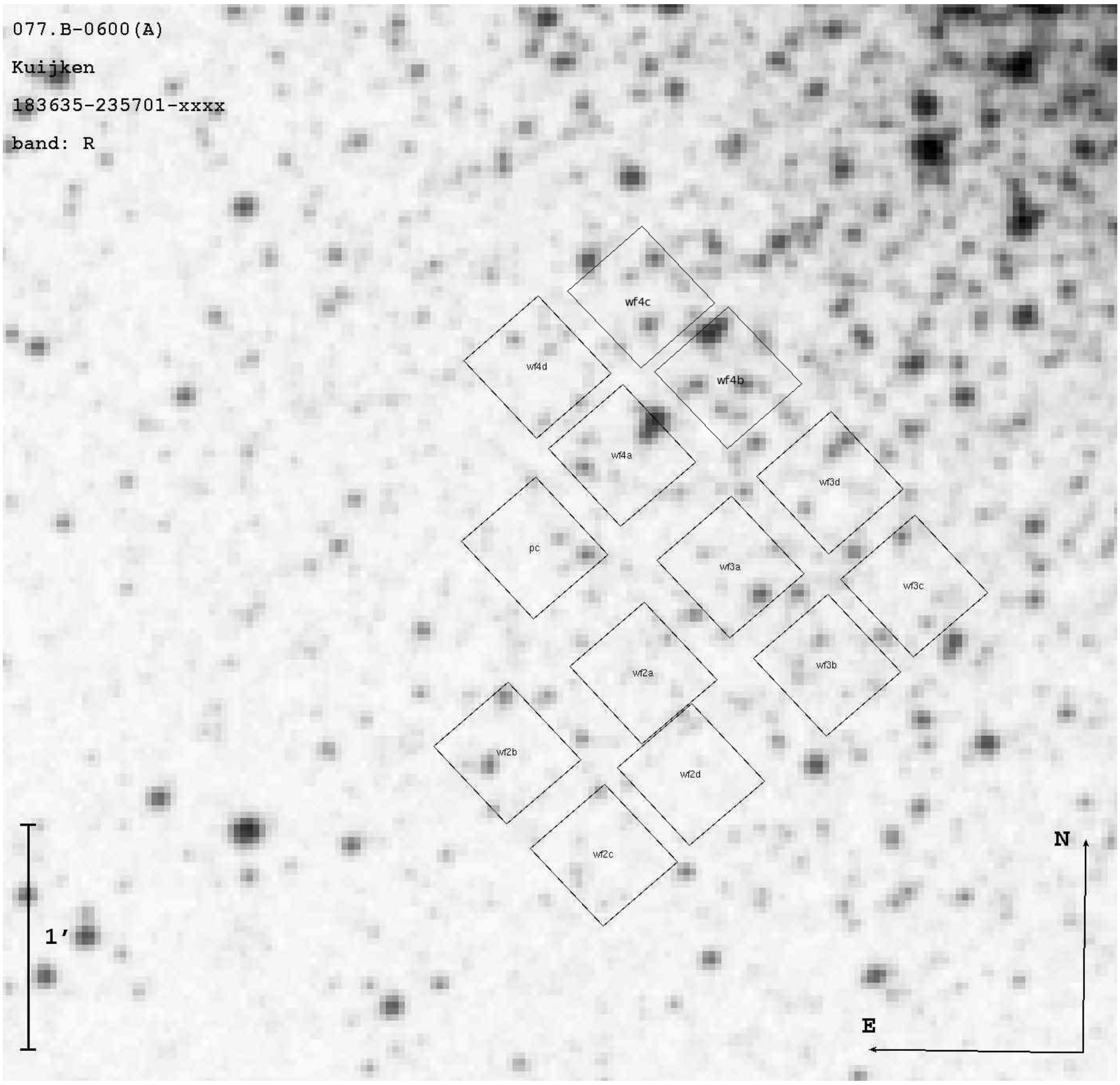

Figure 2.1: The orientation of Field 183635-235701 in respect to the Globular Cluster NGC 6656. Image provided by Mario Soto.

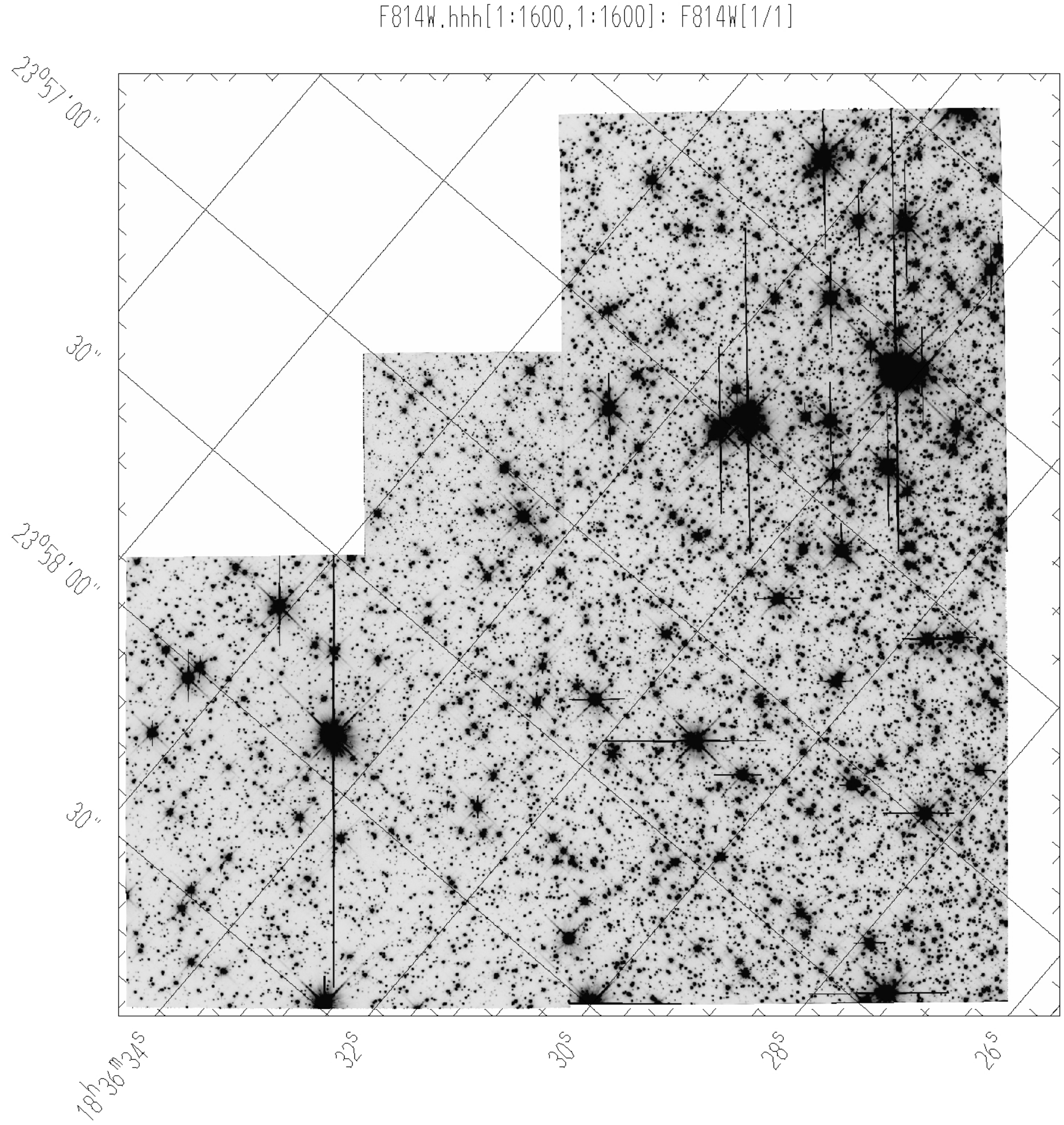

Figure 2.2: Stitched WFPC2 image of Field 183635-235701 in F814W filter.

2.2 The flight-system magnitudes

Because of the long integration time, the brightest stars in the field are saturated and this made photometry of any stars brighter than $V \approx 19.0$ impossible. This would mean that the resulting CMD are truncated some two magnitudes below the turn-off point. Moreover, since this is a crowded area in the direction of the Galactic Bulge, then methods in crowded-field photometry must be employed.

We perform PSF-fitting photometry using the DAOPHOT routine (Stetson, 1987). As a first step, we create a master list of stars to accurately match the stars in two different frames taken by two different filters. With the correct coordinate transform performed by the GEOMAP package in IRAF, we transform the coordinates of images to coordinates of the images in F814W filter. The choice of this filter is simply because previous works that supersedes this work (i.e. Kuijken and Rich (2002)) are all calculated in terms of the positions of objects in the image taken by the F814W filter.

After the proper transformation, we combine all frames regardless of the filter. This step enables us to eliminate the noise produced by cosmic rays as well as the instrument and obtain the highest signal/noise image that can be used to find stars. We run the DAOFIND routine on the median image to obtain the preliminary list of detected stars. DAOFIND works by detecting pixels that are a local density maximum with a certain pre-determined full-width half-maximum (FWHM) and peak amplitude greater than several times the intensity of background sky, denoted σ, which is also pre-determined. To find the best values for the FWHM and σ, we chose several well-isolated stars and measure their FWHM, while σ is determined by measuring the standard deviation of several empty field that is void of any stars. The same set of well-isolated stars are also used to construct a model PSF used in the next phase.

Using ALLSTAR, PSF-fitting photometry is then performed to the list to obtain a cleaner list free from spurious detection of blooming spikes and diffraction rays. To obtain a cleaner list, we then manually remove points detected inside saturated stars and around blooming spikes, since these detected points most certainly are instrument effects. The clean list is then used as input for PHOT to perform aperture photometry on two separate frames of median images taken by the F606W and F814W filter. The count is integrated up to a radius of 3 pixels (corresponding to 138 mas) for the PC1 and 2 pixels (corresponding to 200 mas) for the WFC. The different number is because the images taken by the WFC are more crowded than those taken by the PC1, hence smaller pixel radius was chosen to avoid contamination by nearby stars.

Filter	$\lambda_{\rm mean}(\AA)$	Bandwidth ($\AA$)	$\lambda_{\rm peak}$	UBV analog
F606W	5767	1579.0	6186	Wide V
F814W	8203	1758.0	8387	I

Table 2.1: Broad-band HST filters used in observations. Source: Wide Field and Planetary Camera 2 Instrument Handbook for Cycle 14

2.3 The calibrations

As a first step in calibrating the instrumental magnitude to the standard system, we perform aperture correction on the PC1 and the WFC. This is necessary because we are measuring light intensity on a finite aperture radius, so there is unaccounted light on the wings of the point-spread function. To calculate the correction, we choose several bright and isolated stars on the PC1 and the WFC that are free from light rays of other stars or blooming spikes. We perform aperture photometry of these selected stars up to a radius of 25 pixels (corresponding to 1.15" for the PC1 and 2.5" for the WFC) and plot the growth of the magnitude as the radius increase. Because WF3 and WF4 contain the most stars and are very crowded, it is very hard to find isolated stars. Hence we adopt the values of aperture correction for these chips from the values calculated from WF2, which has a less crowded field.

The calculation of the standard Landolt (1973, 1983) V and I magnitudes depends on true colour the star, which we do not know *a priori*. Thus to capture the standard magnitude $SMAG$ we follow an iterative procedure following the values prescribed by Dolphin (2000):

$$SMAG = -2.5\log(D/t) + Z_{FS} + T_1 SCOL + T_2 SCOL^2 + \Delta Z_{CG}, \tag{2.1}$$

where D is the count in each respective filter, t is the integration time, Z_{FS} is the flight-system zero point discussed in Holtzman et al. (1995) and Whitmore (1995), $T_{1,2}$ are the first and second-order transformation coefficients, and ΔZ_{CG} is the zero-point modification that depends on the chip and gain settings (Dolphin, 2000). The values for each terms can be found on Table 2.2 and Table 2.3. Because of the large color range spanned by the stellar atlas, a single second-order transformation can not fit entire range for all of the filters (Holtzman et al., 1995), hence the last two columns in Table 2.2 give the colour range over which the fits are valid. The iterative procedure began by assuming a certain value of colour index $SCOL$, then calculate the standard magnitude V and I. The result is then used to update the colour index for the next iteration and the calculation is repeated until the difference between successive iterations

Filter	SMAG	SCOL	T_1	T_2	Z_{FS}	$C_{\min}$	$C_{\max}$
F606W	V	$V-I$	0.254	0.012	22.084	...	2.0
F606W	V	$V-I$	-0.247	0.065	22.874	2.0	...
F814W	I	$V-I$	-0.062	0.025	20.827	...	...

Table 2.2: The values for each terms in the calibration process from flight-system magnitudes into standard Landolt magnitudes. $C_{\max}$ is the maximum colour in which the values apply, while $C_{\min}$ is the minimum colour. Source: Dolphin (2000)

Chip	ΔZ_{CG}
PC1	0.701 ± 0.001
WFC2	0.761 ± 0.000
WFC3	0.749 ± 0.000
WFC4	0.722 ± 0.000

Table 2.3: ΔZ_{CG} values for Gain setting = 7. Source: Dolphin (2000)

dropped below 10^{-5}.

Note that there are two different values for the transformations from the F606W filter into the standard V magnitude, which apply in different colour regime. This is indicated in the two last column of the Table 2.2. Should the final standard colour falls outside the regime, we will switch to the other terms and recompute the V magnitude.

2.4 The colour-magnitude diagram

We detected 14577 objects within the field and performed aperture photometry and transformed their flight-system magnitudes into standard magnitudes. The resulting CMD for both bands is shown in Figure 2.3, while the errors of both bands as well as for colours is shown in Figure 2.4. We can see that measurement errors depends heavily on the magnitude of the object. However, most of our measurements are smaller than 0.1 mag and large measurement errors occur only in faint magnitude stars. Comparisons with previous observations of M22 (e.g. Piotto and Zoccali (1999), Monaco et al. (2004)) shows that our measurement is consistent with them, which increase our confidence on the reliability of our measurements. We manage to measure the brightness down to a limiting magnitude of $V \sim 28$. Not unlike the previous works, our

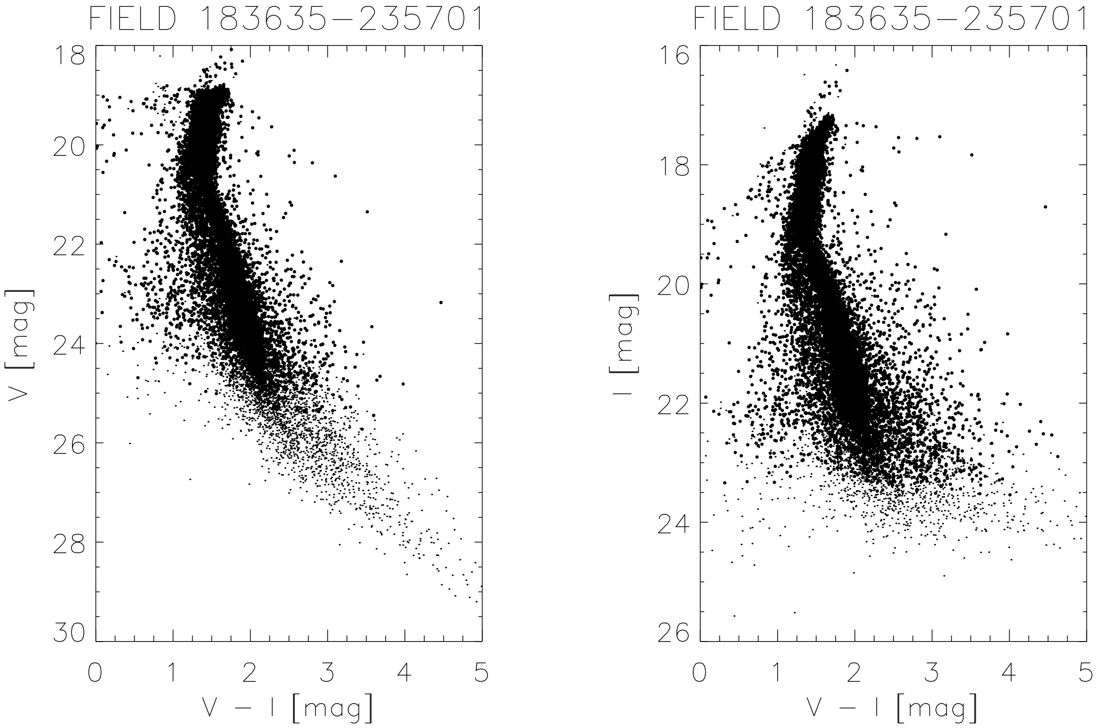

Figure 2.3: The resulting CMD for 14 577 objects in FIELD 183635-235701. Heavier dots correspond to stars with errors better than or equal 0.1 mag. Left is V against colour and right is I against colour.

resulting CMD of the field shows a main sequence structure, presumably are member stars of M22/NGC 6656, and contaminants of field stars, presumably are bulge stars and disc stars. We will discuss on later chapters on how to separate the cluster population with the bulge population.

The high dispersion in the main sequence seen in Figure 2.3 can be interpreted as the internal differential reddening, which upper limit is estimated to be $\langle\sigma_{\mathrm{red}}\rangle \sim 0.05$ mag (Piotto and Zoccali, 1999), or might even be due to chip-to-chip inconsistencies in determining the aperture correction and zero-point modifications. Figure 2.5 plots the CMD of stars in every chips. By comparing the plots in every chips, we can see that the high dispersion are still present in the WF chips, which are more crowded, and we conclude that the chip-to-chip differences are negligible and the high dispersion are mainly caused by the internal reddening within the cluster.

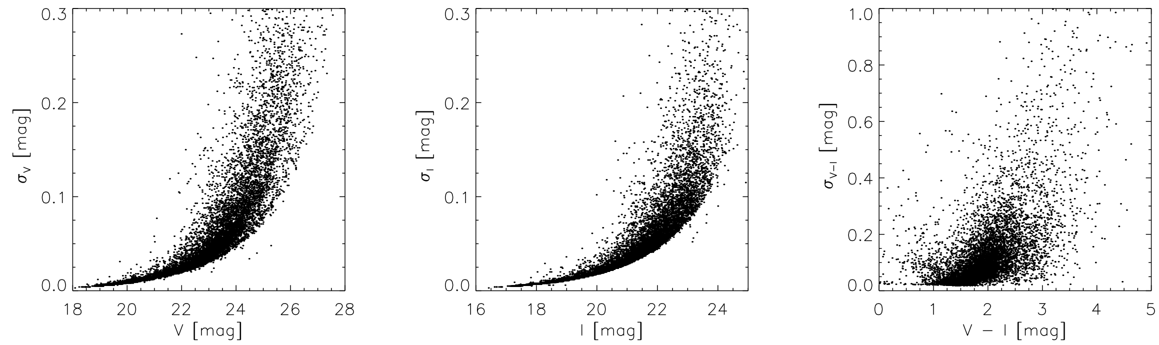

Figure 2.4: The errors of both bands and colours with respect with magnitude.

2.5 The coordinate transformation

By way of DAOFIND and ALLSTAR package, the x-y coordinates of every detected object is also pinpointed. The header of the image records the equatorial coordinates of a reference point in the PC1, as well as the orientation of the camera at the time of integration. Knowing this two parameters as well as the plate scale allow us to make proper transformations from the coordinates in the chip into Equatorial Coordinates. However, since the orientation of the x-y axis of every chip is rotated 90° counter-clockwise with respect to the preceding chip (i.e WF2 is rotated 90° counter-clockwise with respect to PC1, WF3 is rotated 90° counter-clockwise relative to WF2), a proper transformation will be needed to express the x-y coordinates in every chip in terms of PC1. The transformation task using such methods is provided by the METRIC task in the STSDAS package, specifically made to handle images taken with the HST. The result is a set of Equatorial Coordinates for each detected objects with accuracy better than 0.5”. We then transformed this set of coordinates into Galactic Coordinates.

Figure 2.6 displays the position of the 14 577 detected objects in the field, represented in Galactic Coordinates. Several empty spots are apparent in the field, which is due to saturated stars and blooming spikes that prevented detection of any objects around these spots. It should be noted, however, that the transformed coordinates are at the epoch of observations. Should it be necessary, it is trivial to precess the coordinates into standard epoch.

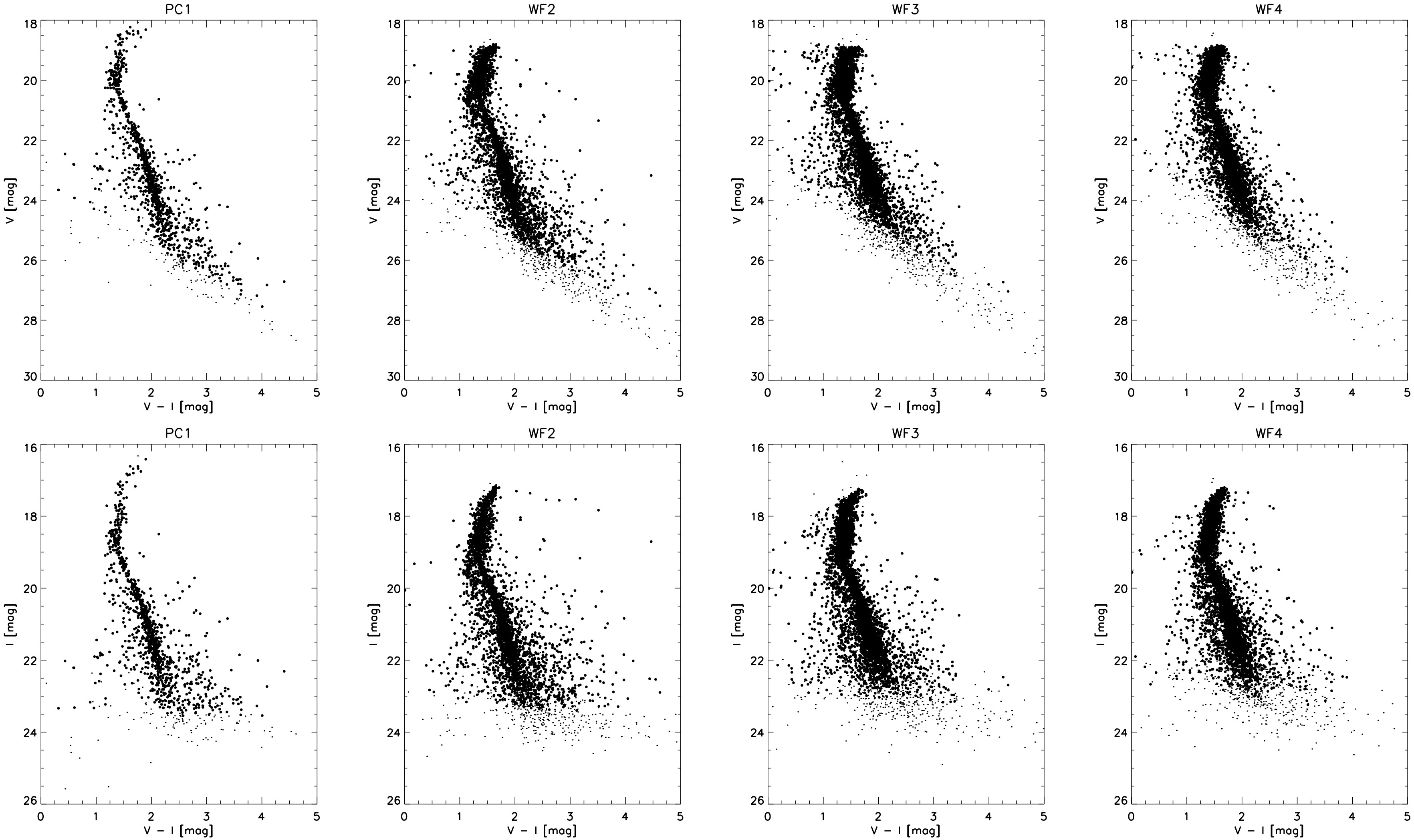

Figure 2.5: Same as in Figure 2.3, but separated into each chips: (from left to right) PC1, WF2, WF3, WF4. The second row plot I magnitude against colour. Heavier dots correspond to stars with errors better than or equal 0.1 mag.

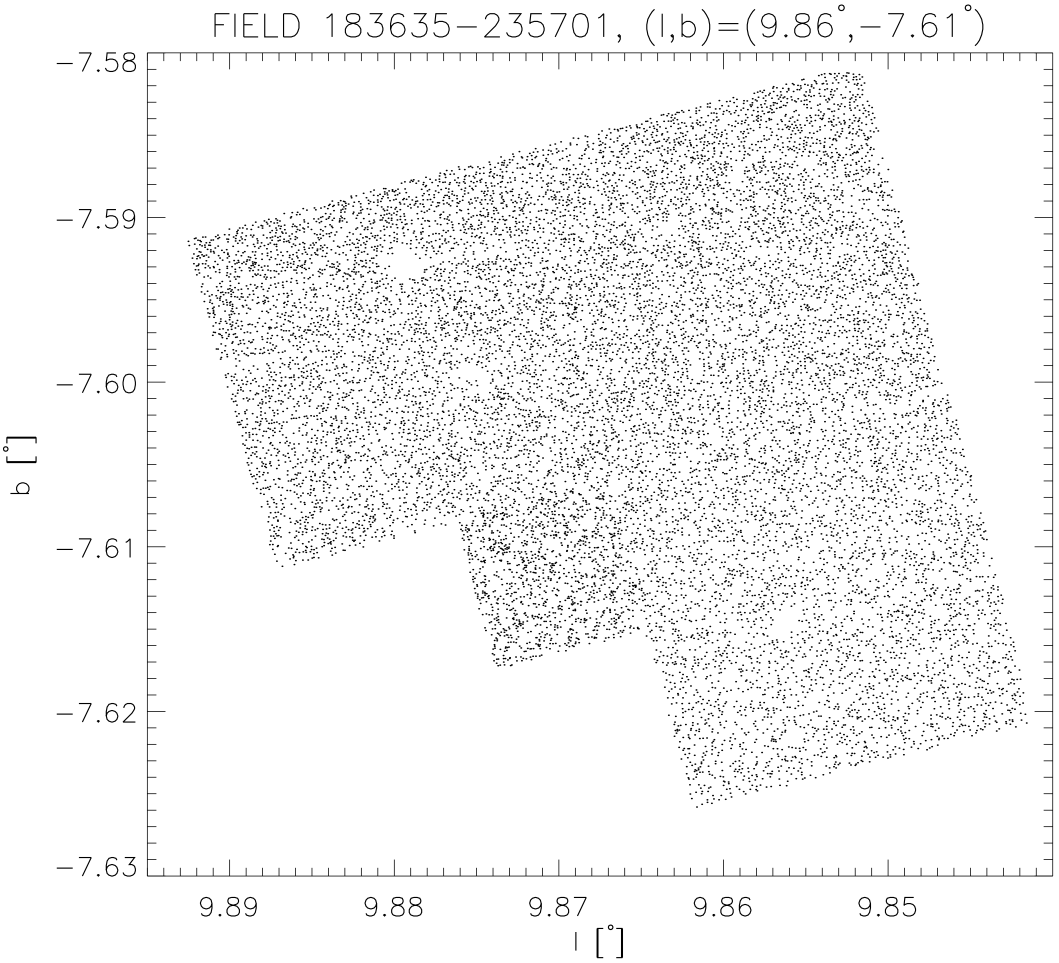

Figure 2.6: The position of 14 577 detected objects in FIELD 183635-235701, shown in Galactic Coordinates. The empty spots in several places are due to saturation of bright stars. WF2 chip is located in the lower-right corner while the WF4 is in the upper-left corner of the plot.

Chapter 3

Proper motions and source-correlation

3.1 The proper motion measurements

In principle, proper motion measurements are conducted by comparing the positions of every detected object in the field between two different epochs. First epoch observations are as described in Section 2.1, while second epoch observations were conducted on 20th of July 2004 with the Advanced Camera for Surveys (ACS) on board the HST. This gave a time span of 9 years which is expected to give a proper motion measurement accuracy up to 0.7 mas yr^{-1} (Kuijken and Rich, 2002). For a distance to the Galactic bulge which is about 8 kpc, this will correspond to 25 km s^{-1}.

After detecting all objects in both epochs with the DAOFIND package, 100 brightest unsaturated stars are chosen to be reference stars. We then use these stars to find an average transformation that maps the stars' position from one epoch to another. This mapping is in the form of polynomial and will predict a star in a given (x, y) position in the chip to its position in the second epoch. The proper motion will then be any position residuals present in the second epoch. Any other residuals that come from systematic errors are also substracted from this position, including pixel phase and "34th row" effect (Anderson and King, 1999). The proper motion measurements are all made by assuming that the mean motion of all stars in the field is zero in both components, thus the measured proper motions are relative. If we want to make an absolute proper motion measurements with respect to an inertial frame of reference, we need extragalactic sources such as QSOs to be present in the field. Future multicolour or spectral studies might be able to provide this reference frame.

3.2 The source-correlation and results

The final output of the previous section is a catalogue of the x-y coordinates of every objects with their detected proper motion in x and y direction. Our next step is obviously then to pull out our photometric catalogue worked-out in Chapter 2 and correlate the sources in both catalogue.

The source-correlating procedure is done by making the x-y coordinates in one list as a reference and then find the nearest object in the second list. Since the proper motion catalogue with 3352 stars is smaller in number than the photometry catalogue (14 577 stars), to ensure a faster calculation we then use the proper motion catalogue as the reference catalogue and then search through the photometry catalogue to look for the closest match within 3 pixels of each stars in the reference catalogue. If within the second list there are no objects within the 3 pixels radius, then the star is thrown away. We also force a one-to-one match in the procedure, in which if there are two or more stars are matched even if they are within the minimum radius, only pairs with the closest distance are kept. This procedure managed to match 2700 stars in both catalogue. These stars form our final catalogue.

The position plot of the 2700 stars is shown in Figure 3.1. There are two marked differences with what is shown in Figure 2.6, the first is the lower density of stars in the field which is due to the fact that not every stars in the field has detectable proper motions. The second, which is more obvious, are the wedge-shaped empty areas. The empty areas are due to the unavailability of second epoch observations conducted with the ACS.

The resulting CMD is shown in Figure 3.2 and Figure 3.3. The majority of stars in our photometric catalogue has been rejected due to scarcity in the proper motion catalogue. However, it is the proper motion data that will be used in separating the globular cluster population with the bulge population. Figure 3.4 displays the proper motion distribution of all the stars in the field as well as in individual WFPC2 chips. A distinct population is apparent which can be kinematically separated.

3.3 The separation of cluster and bulge population

Our attempts in separating the cluster and bulge population begin by a simple assumption that the three-dimensional velocity distribution of a certain population can be represented with a velocity ellipsoid. The velocity ellipsoid is a random distribution represented by the Maxwell-

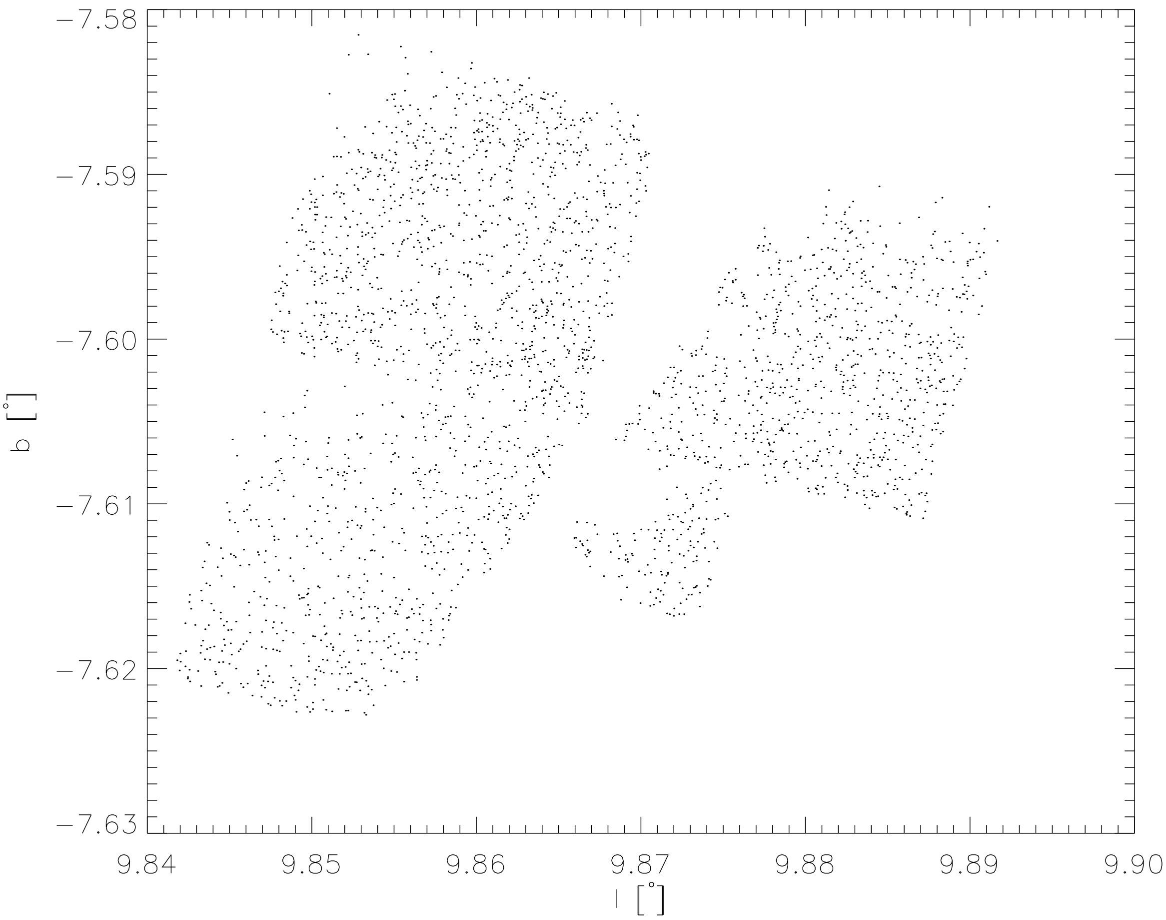

Figure 3.1: The position of 2700 detected objects in FIELD 183635-235701 that have both photometric and proper motion data, shown in Galactic Coordinates. The wedge-shaped empty areas are due to the fact that those areas are not observed by the second epoch observation by ACS (Advanced Camera for Surveys) WF2 chip is located in the lower-right corner while the WF4 is in the upper-left corner of the plot.

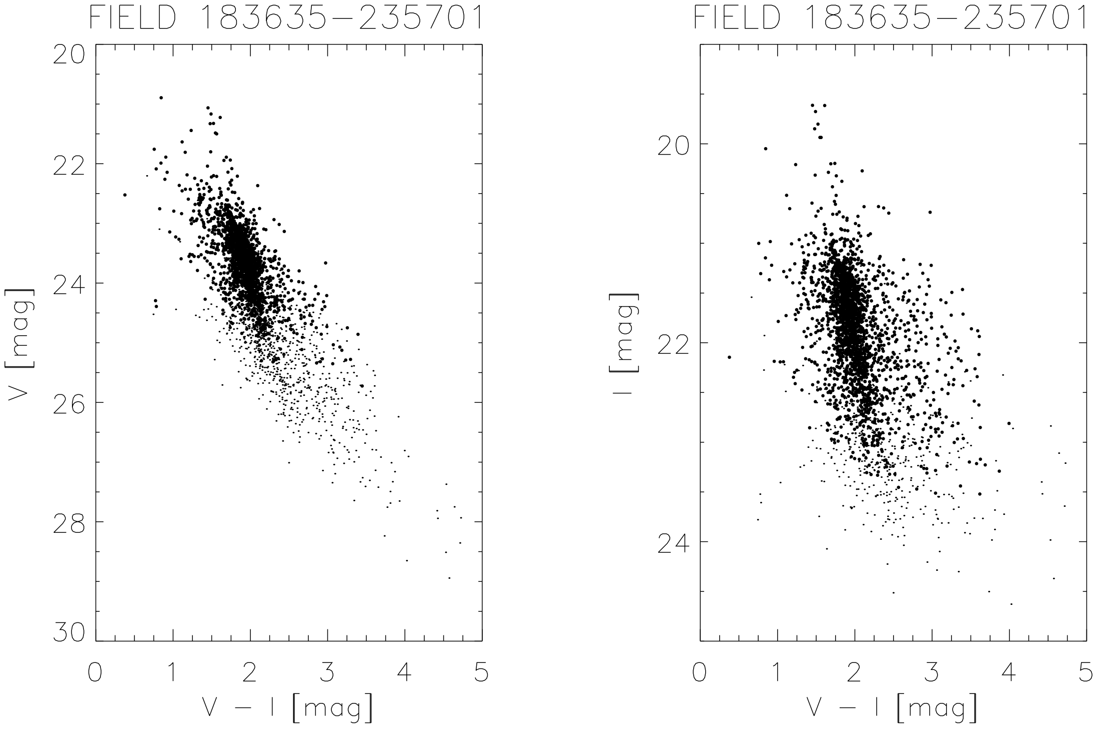

Figure 3.2: Colour-Magnitude diagram for 2700 source-correlated stars. The stars in this diagram have photometric as well as kinematical data. Heavier dots correspond to photometric errors better than or equal to 0.1 mag. Left is V against colour and right is I against colour.

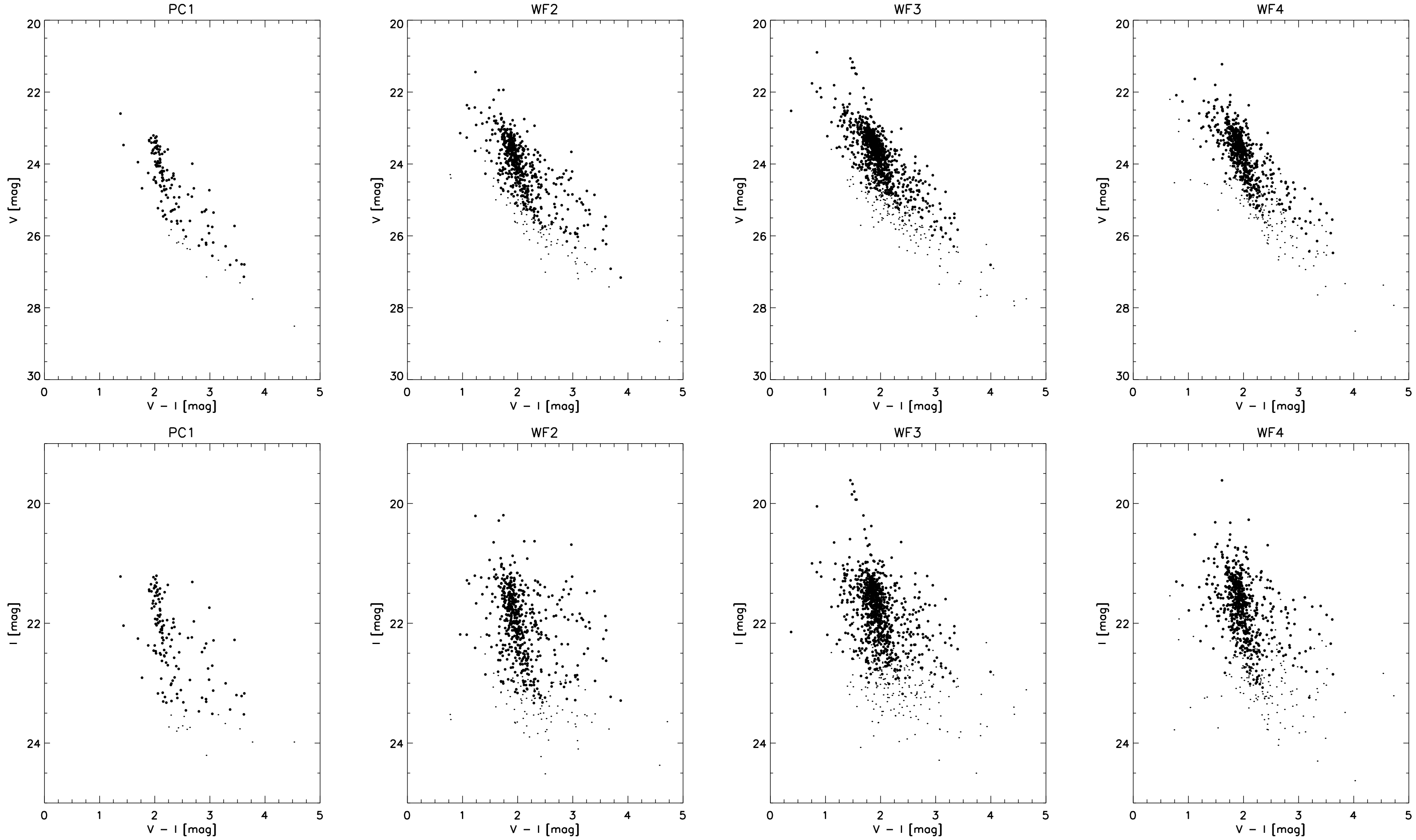

Figure 3.3: Same as in Figure 3.2, but the stars are separated into their position in the WFPC2 chips. The top row is V against colour and the bottom row is I against colour. Heavier dots correspond to stars with photometric errors better than or equal to 0.1 mag.

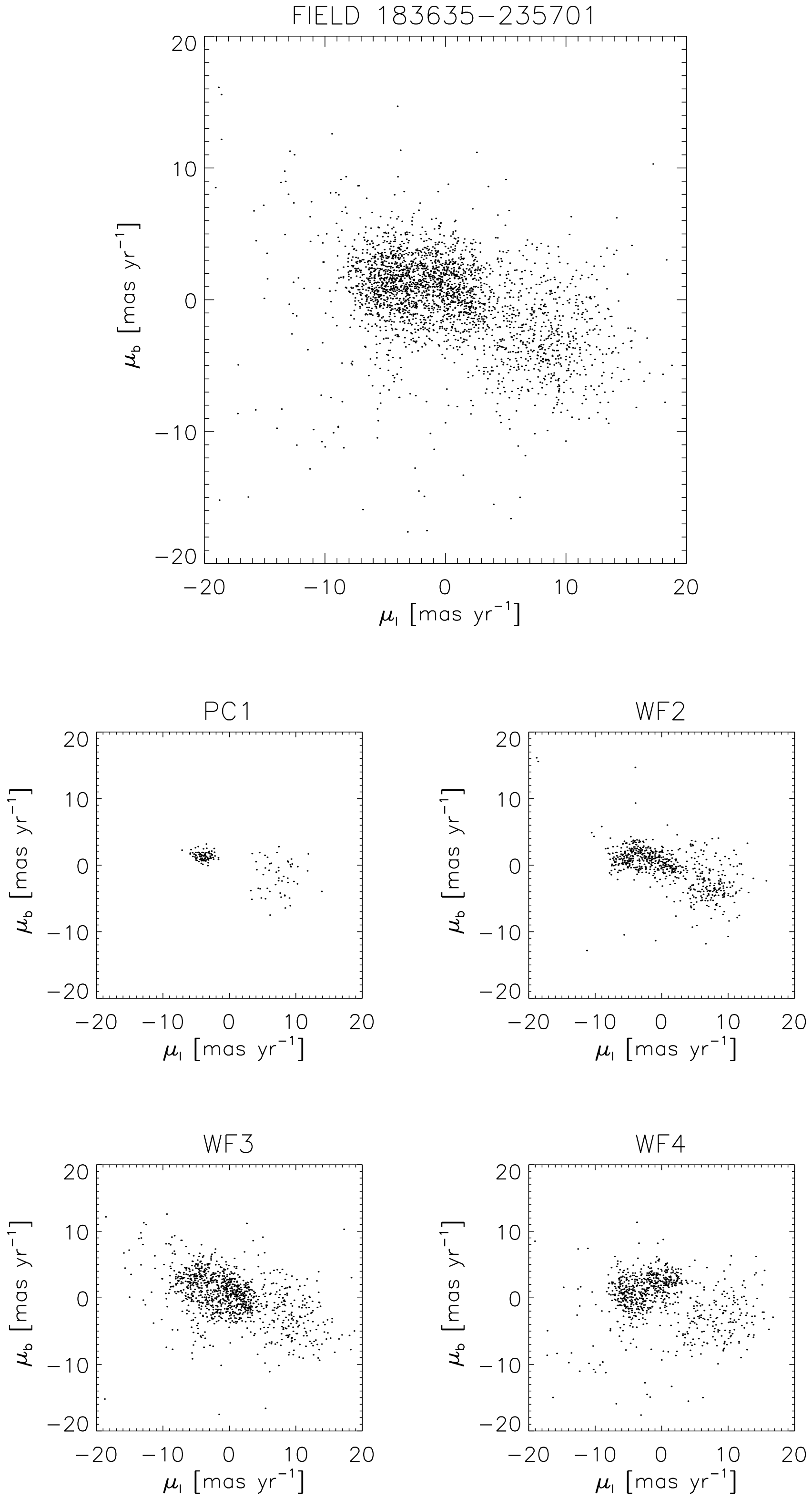

Figure 3.4: The proper motion distribution of all stars in the field and within the individual chips.

Boltzmann distribution

$$\mathrm{d}n \propto \exp\left[-\left(\frac{v_1^2}{2\sigma_1^2}+\frac{v_2^2}{2\sigma_2^2}+\frac{v_3^2}{2\sigma_3^2}\right)\right]\mathrm{d}v_1\mathrm{d}v_2\mathrm{d}v_3, \tag{3.1}$$

which center of ellipsoid (v_1, v_2, v_3) is the mean velocity of the population and $(\sigma_1, \sigma_2, \sigma_3)$ is the velocity dispersion in the direction of each axis represented by the length of the semimajor axes of the ellipsoid. The situation could be made more complex if the ellipsoid itself is oriented at a certain oblique angle from the chosen axis. Figure 3.5 illustrate such three-dimensional velocity ellipsoid.

Since our data contains only two components motion instead of three, then the velocity distribution is a projection of the ellipsoid into the plane of proper motion. The projected shape is then an ellipse instead of an ellipsoid which center (v_1, v_2) is the mean motion of the group, (σ_1, σ_2) is the velocity dispersion, and θ is the obliquity of the ellipse. The amplitude of Equation 3.1 should also be taken into account. Hence, there are 6 parameters that describe the velocity distribution of a stellar population.

In Figure 3.4 we can already distinguish two different set of populations by their kinematics. The next step is then to describe both populations in terms of the parameters of their own velocity ellipsoid. We do this by fitting our proper motion data with a bivariate bimodal Gaussian function

$$f(v_x, v_y) = c_1 \exp\left[-\frac{1}{2}\left\{\left(\frac{v'_{x,1}}{\sigma_{x,1}}\right)^2+\left(\frac{v'_{y,1}}{\sigma_{y,1}}\right)^2\right\}\right]+c_2 \exp\left[-\frac{1}{2}\left\{\left(\frac{v'_{x,2}}{\sigma_{x,2}}\right)^2+\left(\frac{v'_{y,2}}{\sigma_{y,2}}\right)^2\right\}\right], \tag{3.2}$$

where $(v'_{x,1}, v'_{y,1})$ and $(v'_{x,2}, v'_{y,2})$ is the rotated points in the velocity space according to the angle θ_1 and θ_2, respectively:

$$\begin{bmatrix} v'_{x,1} \\ v'_{y,1} \end{bmatrix} = \begin{bmatrix} \cos\theta_1 & -\sin\theta_1 \\ \sin\theta_1 & \cos\theta_1 \end{bmatrix} \begin{bmatrix} v_x - \bar{v}_{x,1} \\ v_y - \bar{v}_{y,1} \end{bmatrix} \tag{3.3a}$$

$$\begin{bmatrix} v'_{x,2} \\ v'_{y,2} \end{bmatrix} = \begin{bmatrix} \cos\theta_2 & -\sin\theta_2 \\ \sin\theta_2 & \cos\theta_2 \end{bmatrix} \begin{bmatrix} v_x - \bar{v}_{x,2} \\ v_y - \bar{v}_{y,2} \end{bmatrix} \tag{3.3b}$$

Hence the function has 12 parameters $(\bar{v}_{x,1}, \bar{v}_{y,1}, \sigma_{x,1}, \sigma_{y,1}, \theta_1, c_1, \bar{v}_{x,2}, \bar{v}_{y,2}, \sigma_{x,2}, \sigma_{y,2}, \theta_2, c_2)$ that have to be solved simultaneously. By binning our proper motion data in a 1×1 mas yr^{-1} bin, we then seek the 12 parameters by performing the Levenberg-Marquardt algorithm to fit our data to Equation 3.2. We used the unrotated (μ_x, μ_y) data for our initial fitting, and use the results (Table 3.1) to pick out stars from each population within 1σ of the velocity ellipse. In Figure 3.6, we show the CMD of both populations as well as the position of the selected stars

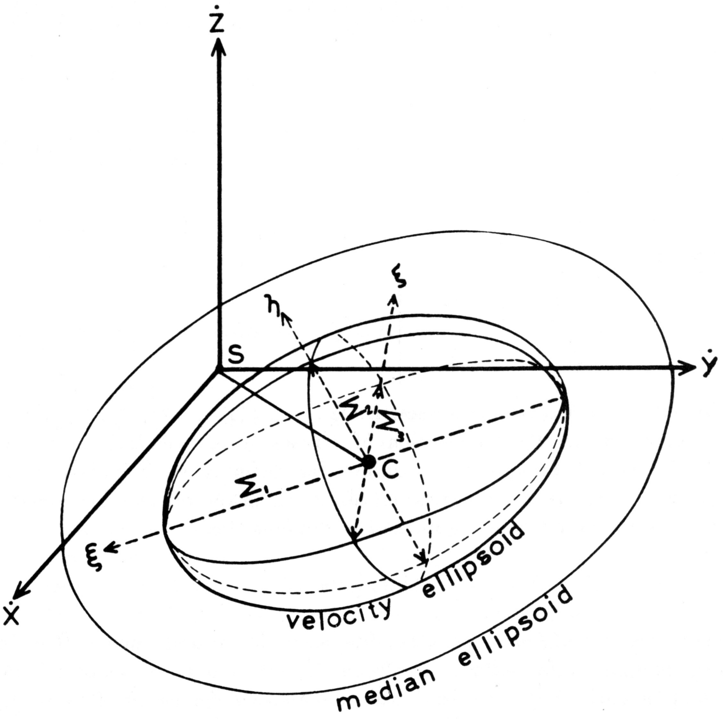

Figure 3.5: The Schwarzschild velocity ellipsoid describing velocity distribution in velocity space. Source: Trumpler and Weaver (1953)

in the proper motion distribution. Stars marked in red are members of NGC 6656 while stars marked in blue are members of the bulge population.

3.4 The removal of residuals in the proper motions

Figure 3.7 shows the relation of proper motions in the x-y coordinates according to their position in the chip. We can see that there are systematic relations between proper motions and position. These are traces of systematic residuals that are still present in the proper motion data and has to be corrected. We deduce that these residuals came from the fact that our assumption that the mean motion of the stars are zero is not correct, because the field is also contaminated by stars from the cluster which also has their own motion. Thus the average motion is not zero.

However, if we use the member stars of NGC 6656 as frame of reference and assuming that their mean motion are constant anywhere, we can remove this residual if we then measure the proper motion with respect to the cluster. The corrections in each chip were first done by selecting member stars of NGC 6656 using the Gaussian fitting described in Section 3.3. We

Population	c	$\bar{\mu}_x$	$\bar{\mu}_y$	σ_x	σ_y	θ
NGC 6656	41.87	1.95	1.87	1.97	3.64	25.28
Bulge	10.13	-5.38	-6.18	2.80	3.89	25.10

Table 3.1: The parameters of the two velocity ellipse for NGC 6656 and the bulge population, calculated by fitting a bivariate bimodal Gaussian function to the proper motion data. c is the amplitude of the Gaussian function.

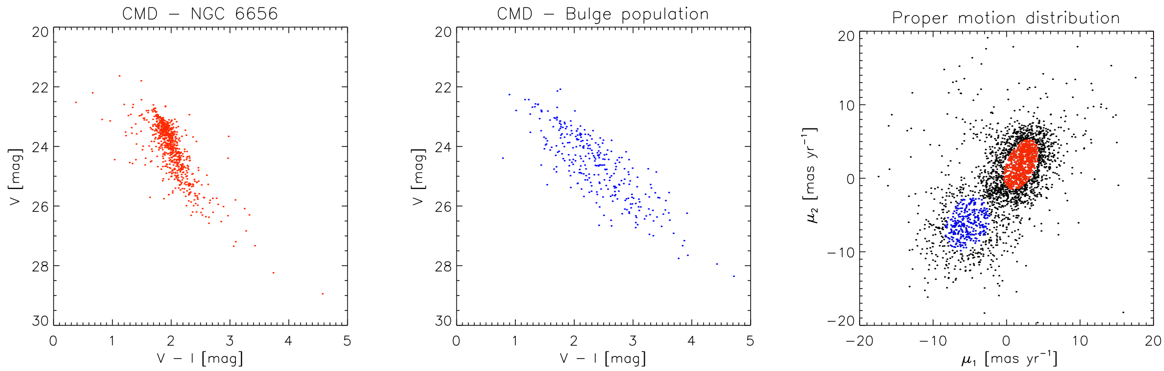

Figure 3.6: The CMD for stars in NGC 6656 and members of the bulge population, selected by drawing 1σ velocity ellipse in the proper motion distribution and take all stars within the ellipse. Red denotes members of NGC 6656 and blue denotes members of the bulge population.

then fit these selected member stars to a two-dimensional polynomial of order 3 in the form

$$\mu = \sum_{i,j=0}^{3} k_{ij} x^i y^j, \tag{3.4}$$

from which the results are used to calculate the amount of correction that need to be added to each star on the chip. For each chip there are two forms of Equation 3.4, one for μ_x and one for μ_y, both as a function (x, y). By setting the mean proper motions of the cluster as zero in both components, the amount of correction is simply the value of Equation 3.4 in a given (x, y) coordinates of the star in question. Figure 3.8 describes the polynomial fitting for each chips and the values of μ_x and μ_y in each chips before and after corrections. We can see that there are still a slight residual in several chips even after correction. Hence we iterate the process up to the fifth time. From Figures 3.8 to 3.12 we can see that the iteration process gradually diminish the residuals in the proper motion. In Figure 3.13 we can track the change of proper motion distribution after each succesive iteration. Most outliers in the proper motion distribution in fact get corrected so that they move closer to the center of distribution. After the second iteration, the correction looked like it has stabilised to near-zero and further iterations seem like a redundant step. However, this might not be the case since Figures 3.8 to 3.12 indicate that corrections well into fifth iteration are necessary for positions close to the edge of WF3 and WF4 chips.

3.5 Final results

Having applied the necessary corrections for the proper motions, we then transformed the proper motion components into (μ_l, μ_b). Figure 3.14 shows the overall proper motion distribution in the field as well as in every chip.

Using this corrected proper motion data, we then construct binned colour-magnitude diagrams of the stars in the field to see whether their kinematical quantities correlate with their position in the CMD. In Figure 3.15 we show the binned CMD. There are a clear separation between cluster stars and bulge stars. Because we have already set the mean motion of cluster stars to be zero, we can see in the binned CMD that calculates the mean motion in l, which stars are members of the cluster and which are members of the bulge.

To see whether there are any correlation between kinematical quantities with the stars' position in the sky, we also binned the stars in their galactic coordinates and calculate each stars mean motion and dispersion in each bin. Figure 3.16 shows such diagram. In this plot we can discern the groupings of cluster members and bulge population by comparing the mean motion plots with the mean motions in Figure 3.15.

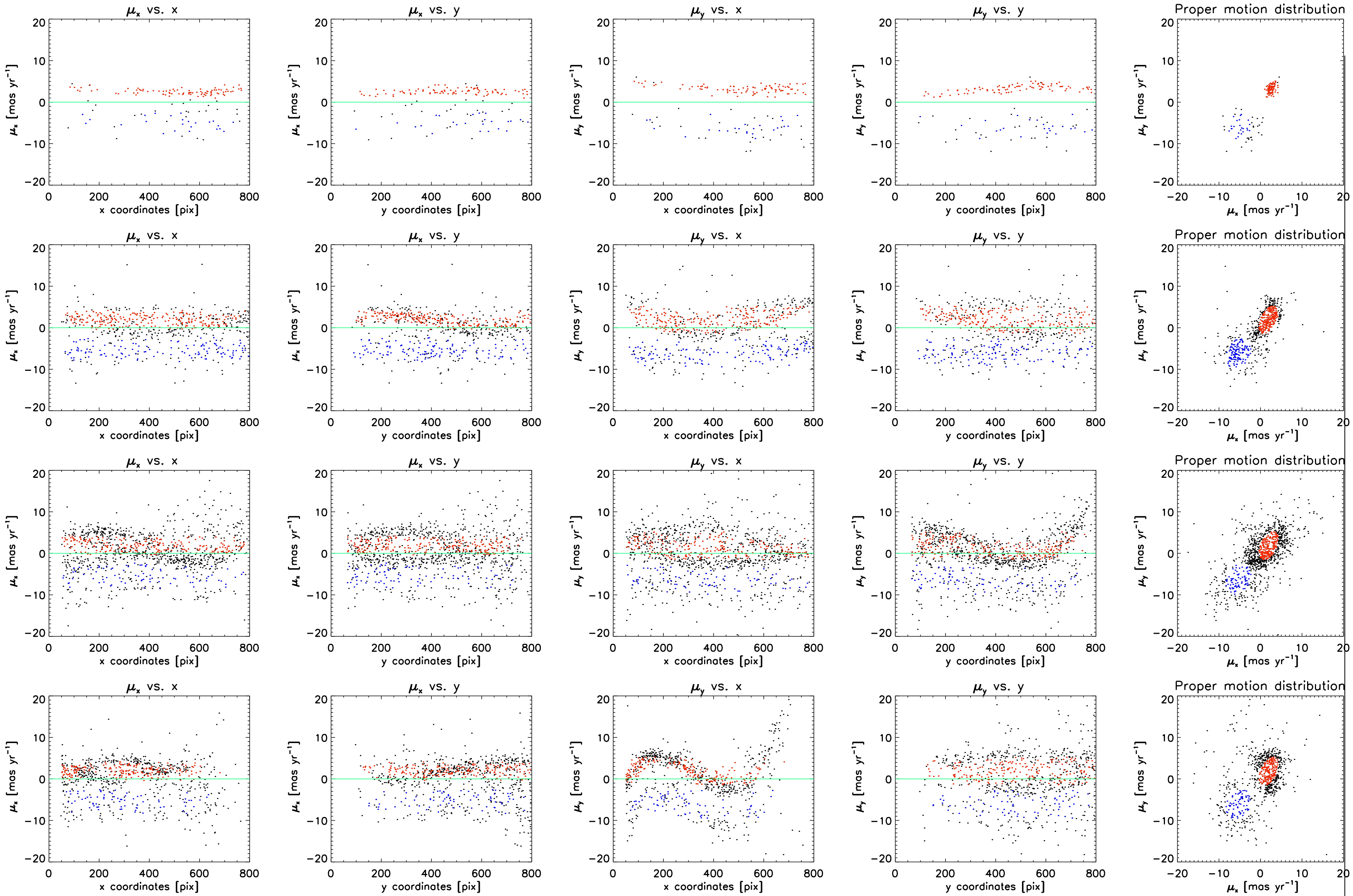

Figure 3.7: The relation of proper motions in each chip with their x-y coordinates in the chip. First row: PC1, second row: WF2, third row: WF3, fourth row: WF4.

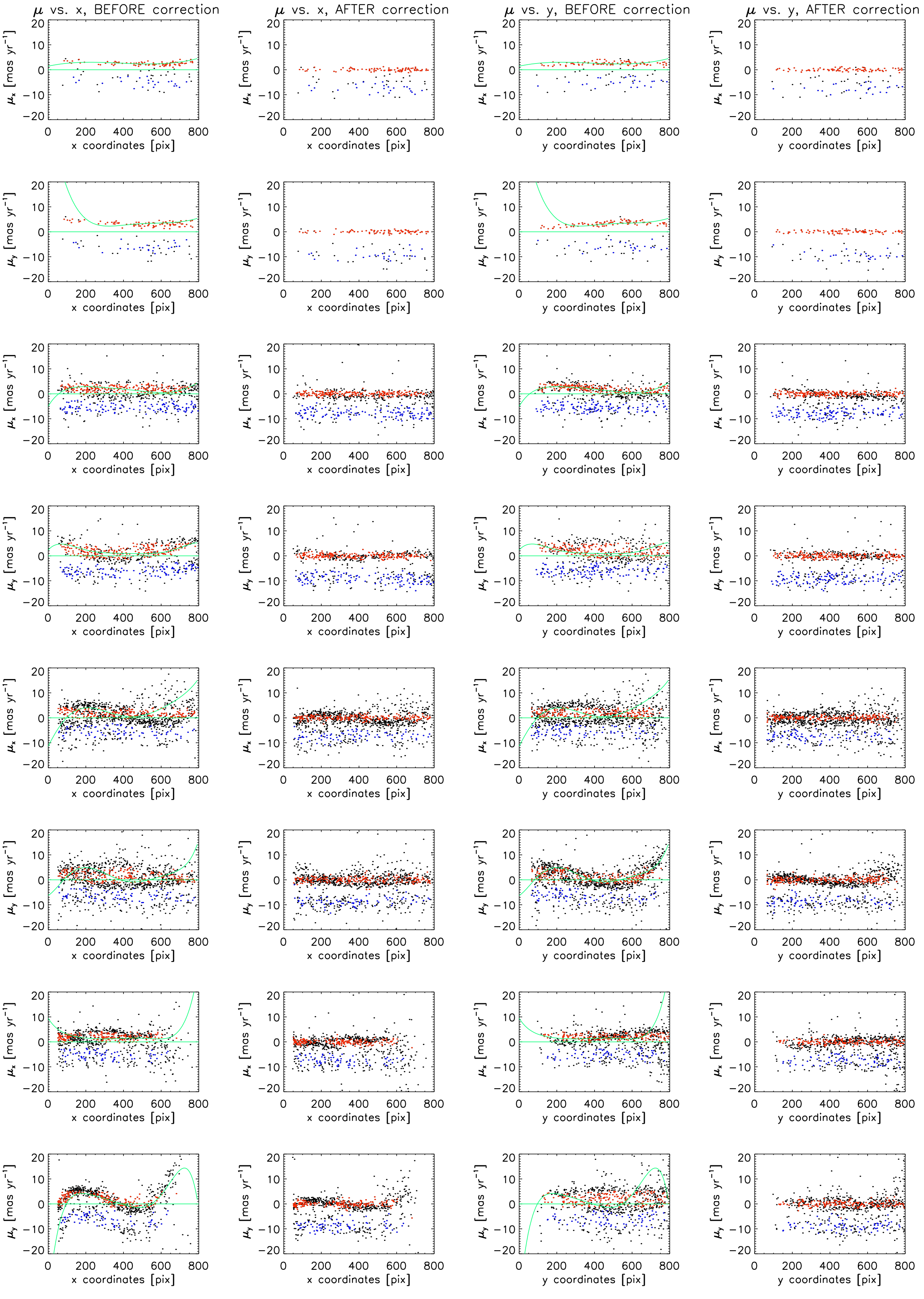

Figure 3.8: The corrections of proper motion for each chip. Row 1-2: PC1, row 3-4: WF2, row 5-6: WF3, row 7-8: WF4. Column 1-2: Before-and-after correction plot for μ_x vs. x coordinates (first row) and μ_y vs. x coordinates (second row), Column 3-4: Before-and-after correction plot for μ_y vs. y coordinates (first row) and μ_y vs. y coordinates (second row). Green curves indicate the result of the two-dimensional polynomial fitting to the cluster members.

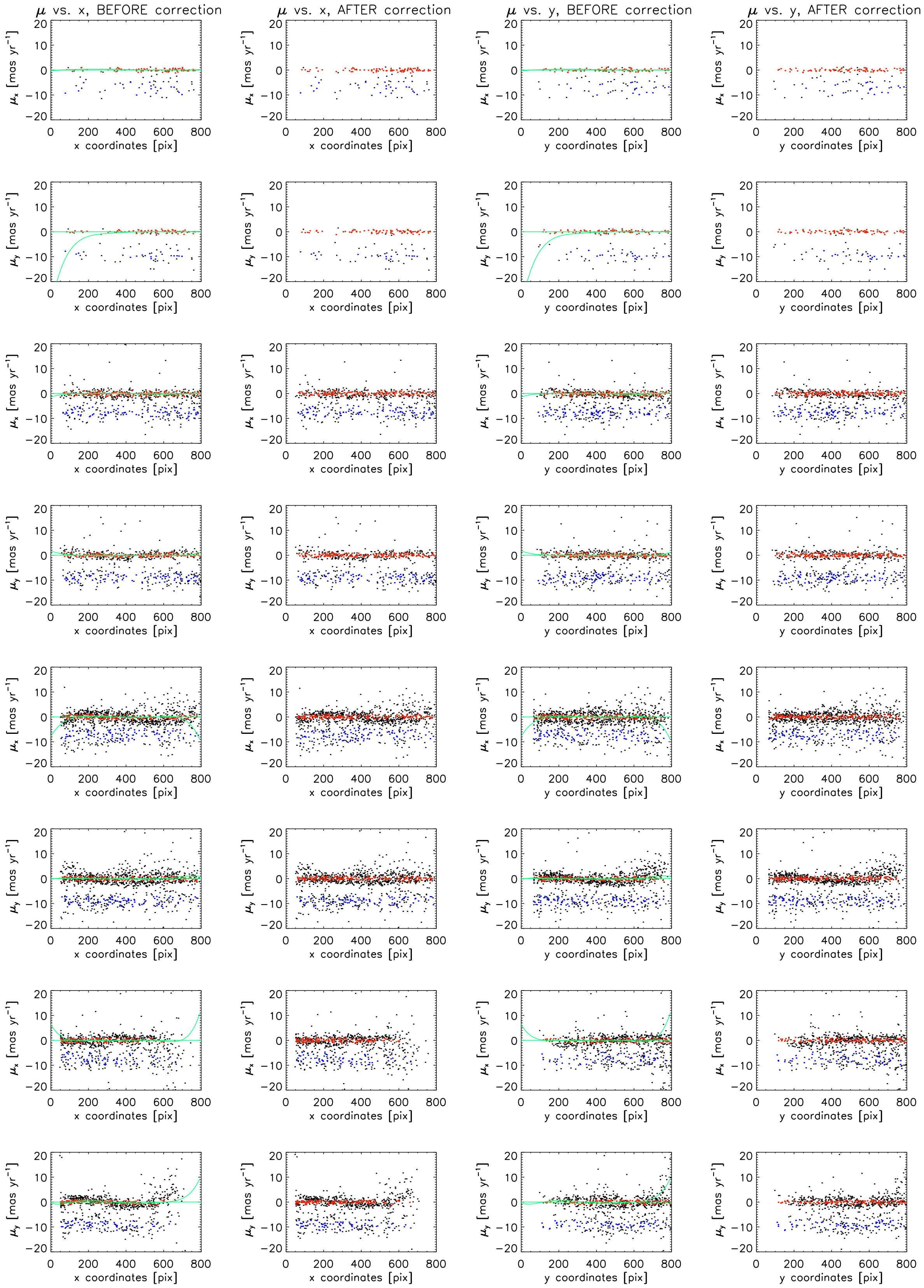

Figure 3.9: Same as in Figure 3.8, but for the second iteration.

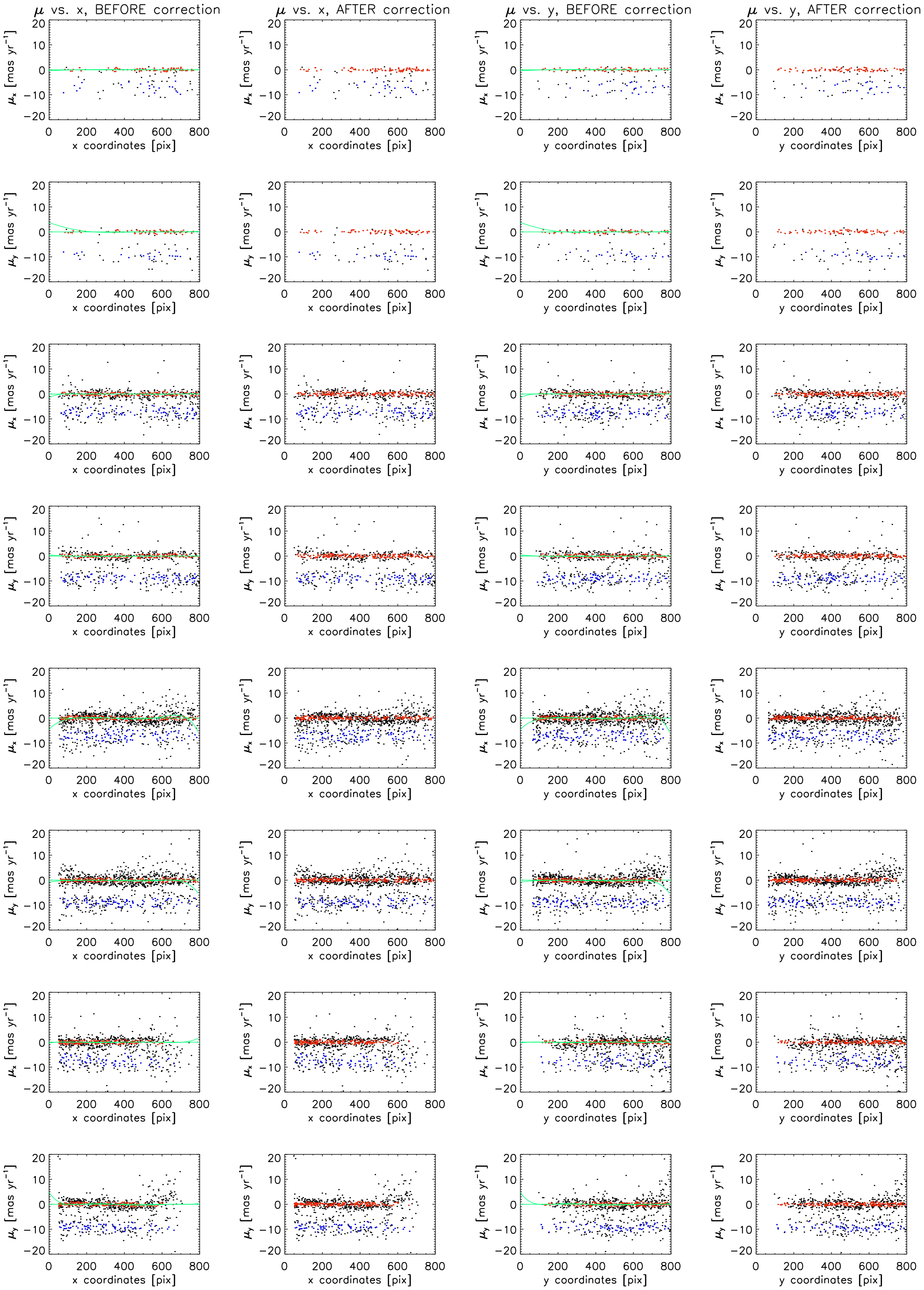

Figure 3.10: Same as in Figure 3.8, but for the third iteration.

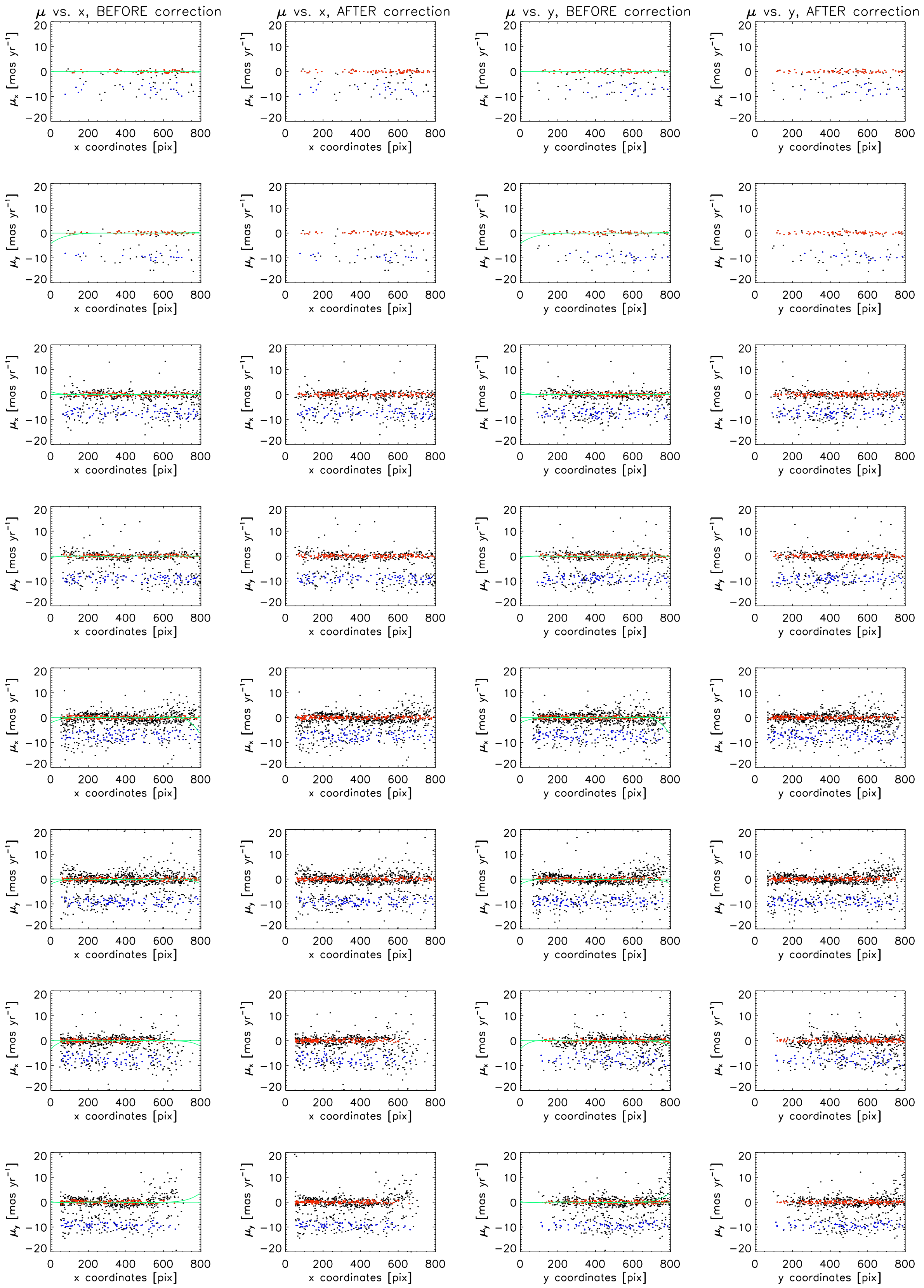

Figure 3.11: Same as in Figure 3.8, but for the fourth iteration.

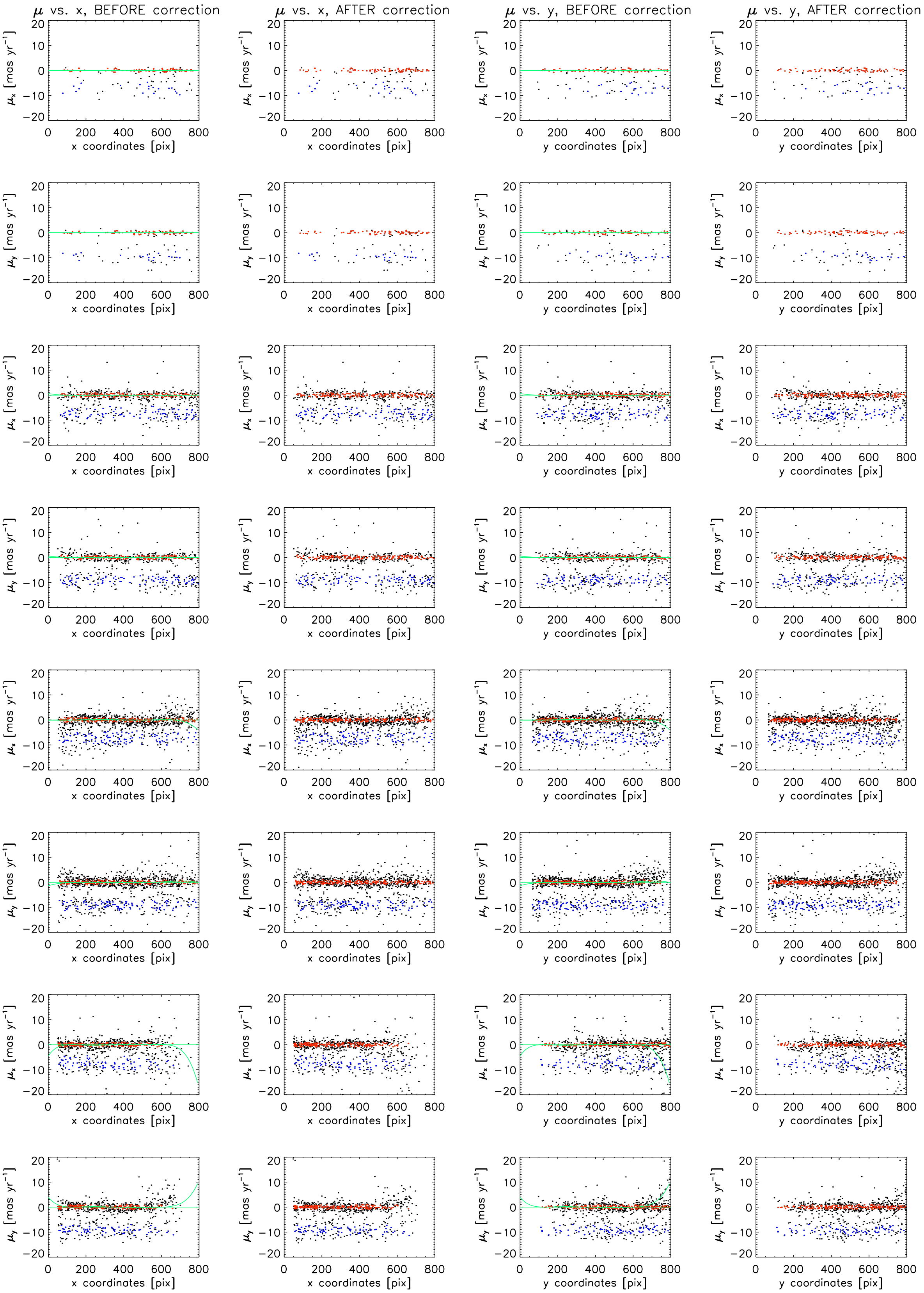

Figure 3.12: Same as in Figure 3.8, but for the fifth iteration.

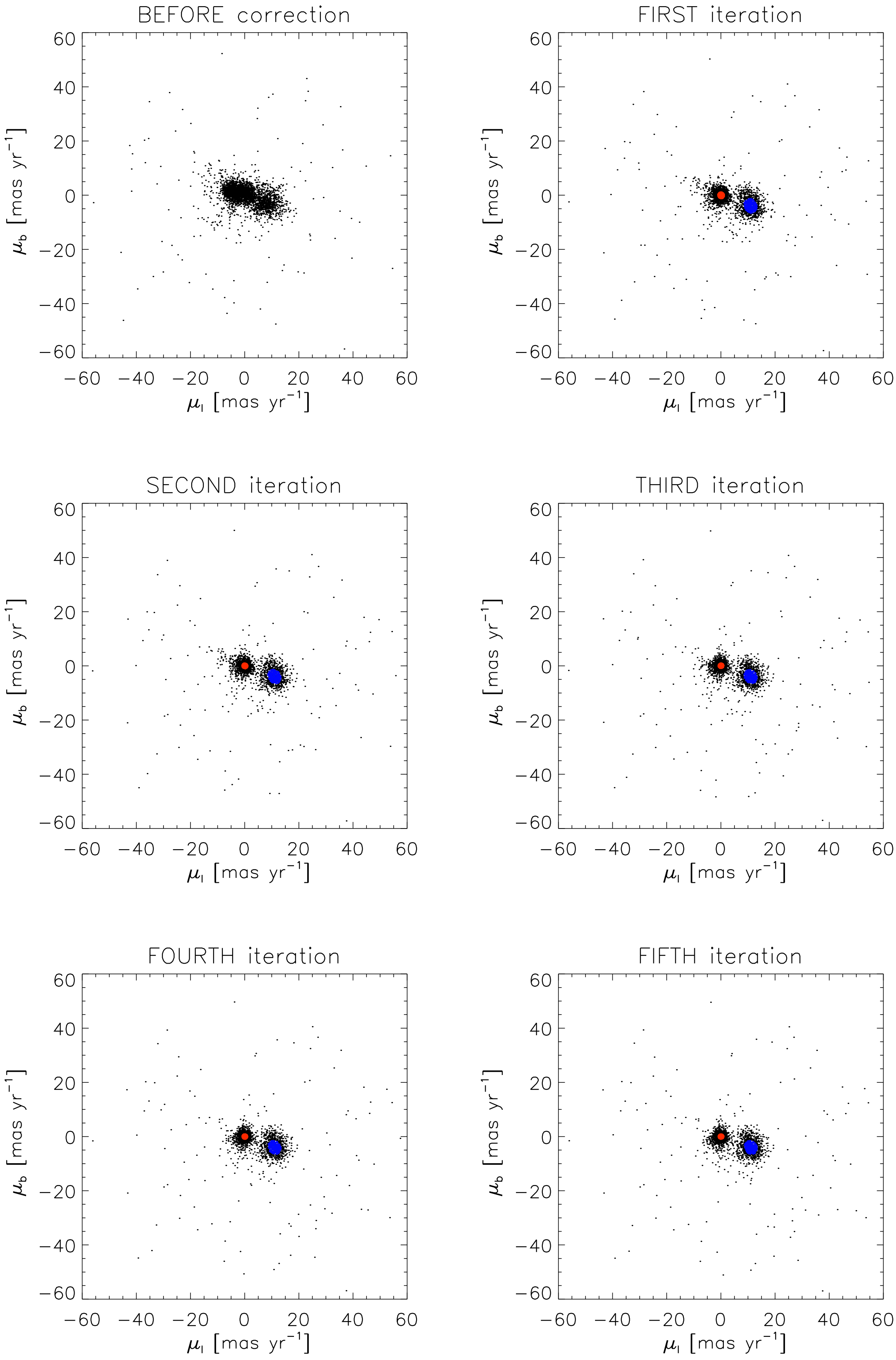

Figure 3.13: The change of proper motion distribution of all stars in the field, after each successive iteration. Red-colored stars are presumed members of the cluster while blue-colored stars are presumed members of the bulge population, both selected by calculating their ellipse parameters after each iteration and pick stars within 1σ of the velocity ellipse.

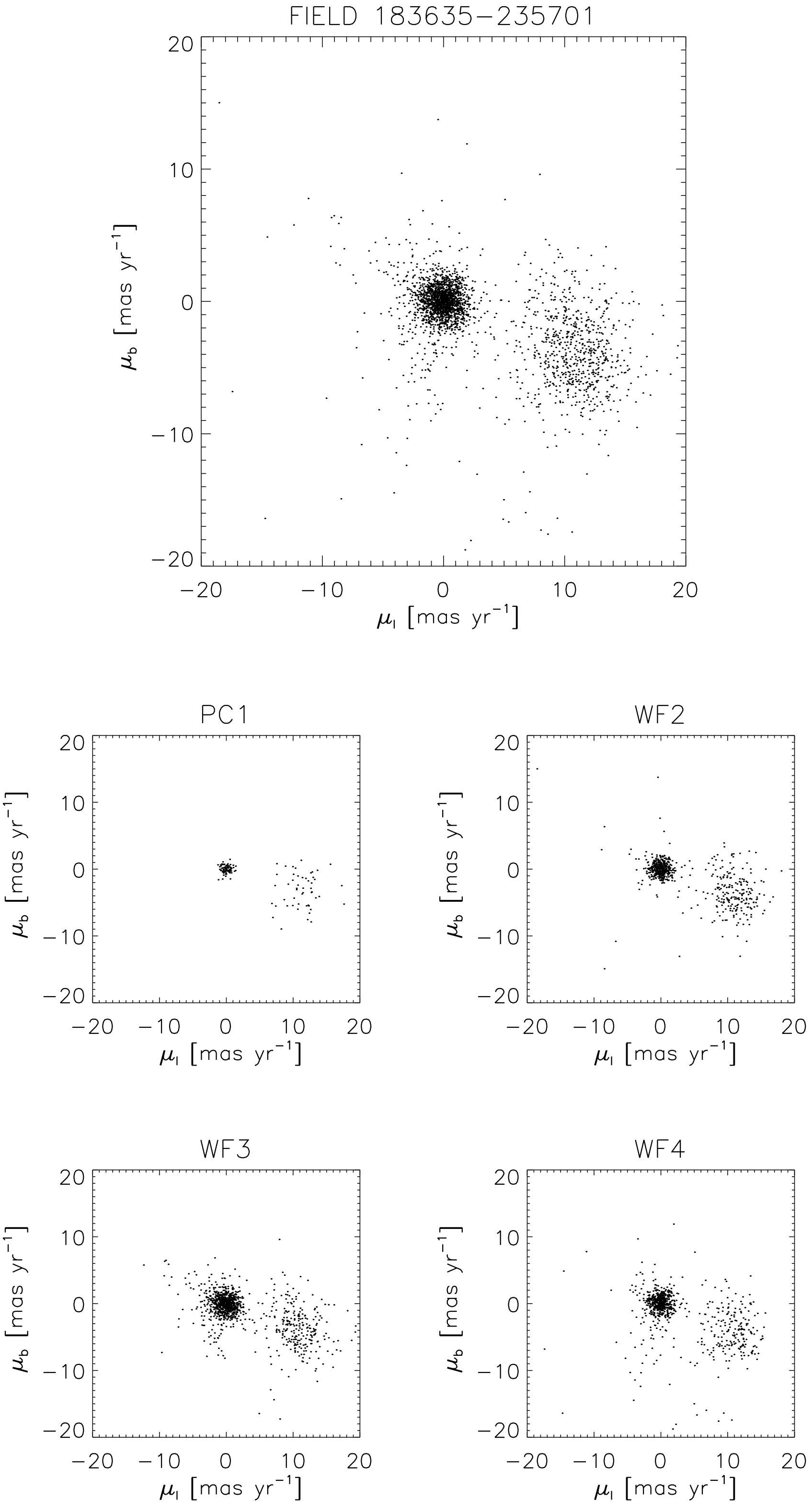

Figure 3.14: The proper motion distribution of all stars in the field and within the individual chips after correction has been applied.

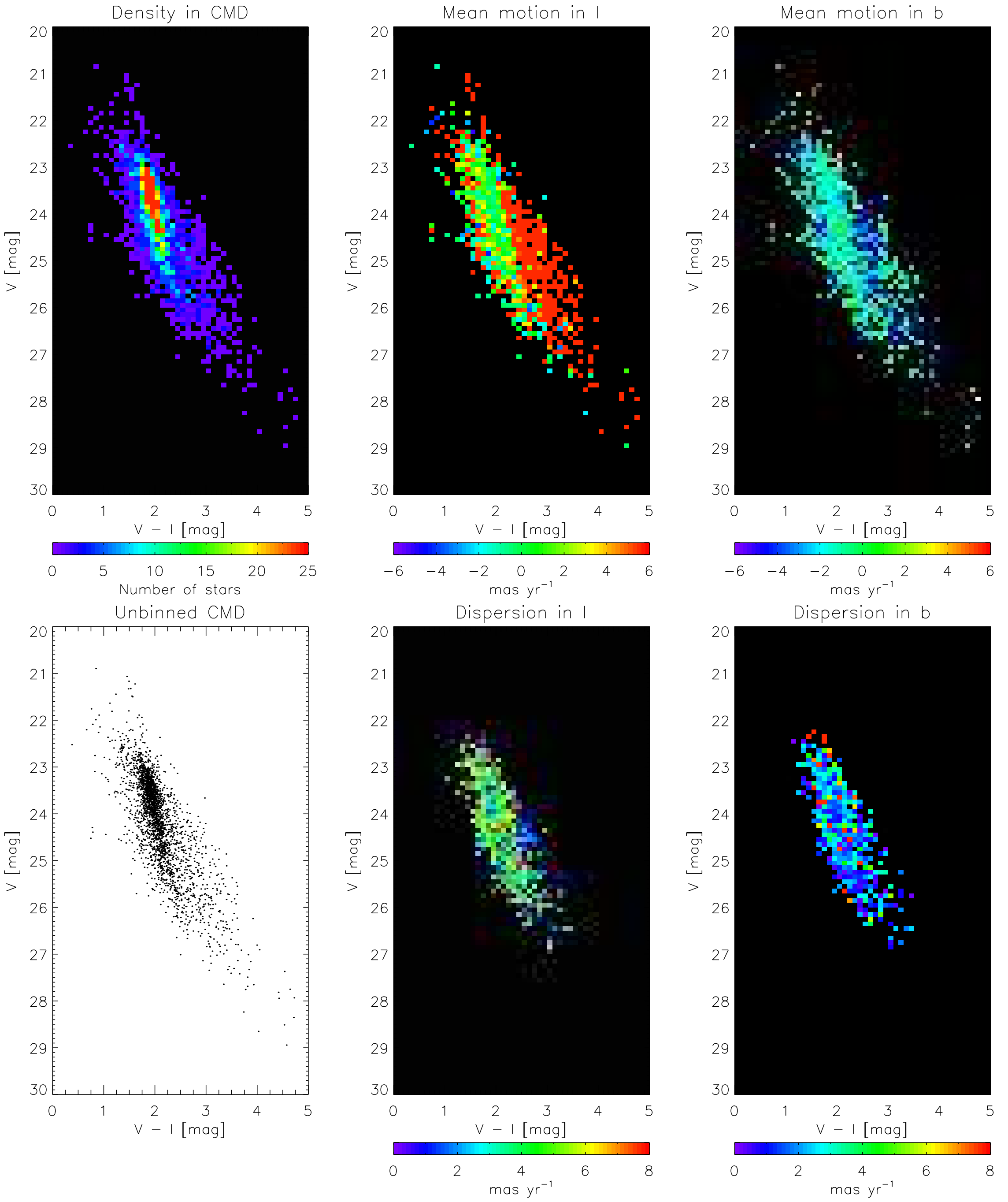

Figure 3.15: Binned CMD for the stars in Field 183635-235701. The sample is binned in 0.1 × 0.1 mag box and colour-coded in schemes according to the legend in the bottom of each plot. *Top row, left to right:* Number of stars in each bin, mean motion in l direction, mean motion in b direction. *Bottom row, left to right:* Unbinned CMD, velocity dispersion in l direction, velocity direction in b direction. In the plot of mean motion we can see that there is clear separation between the population of the globular cluster and the bulge.

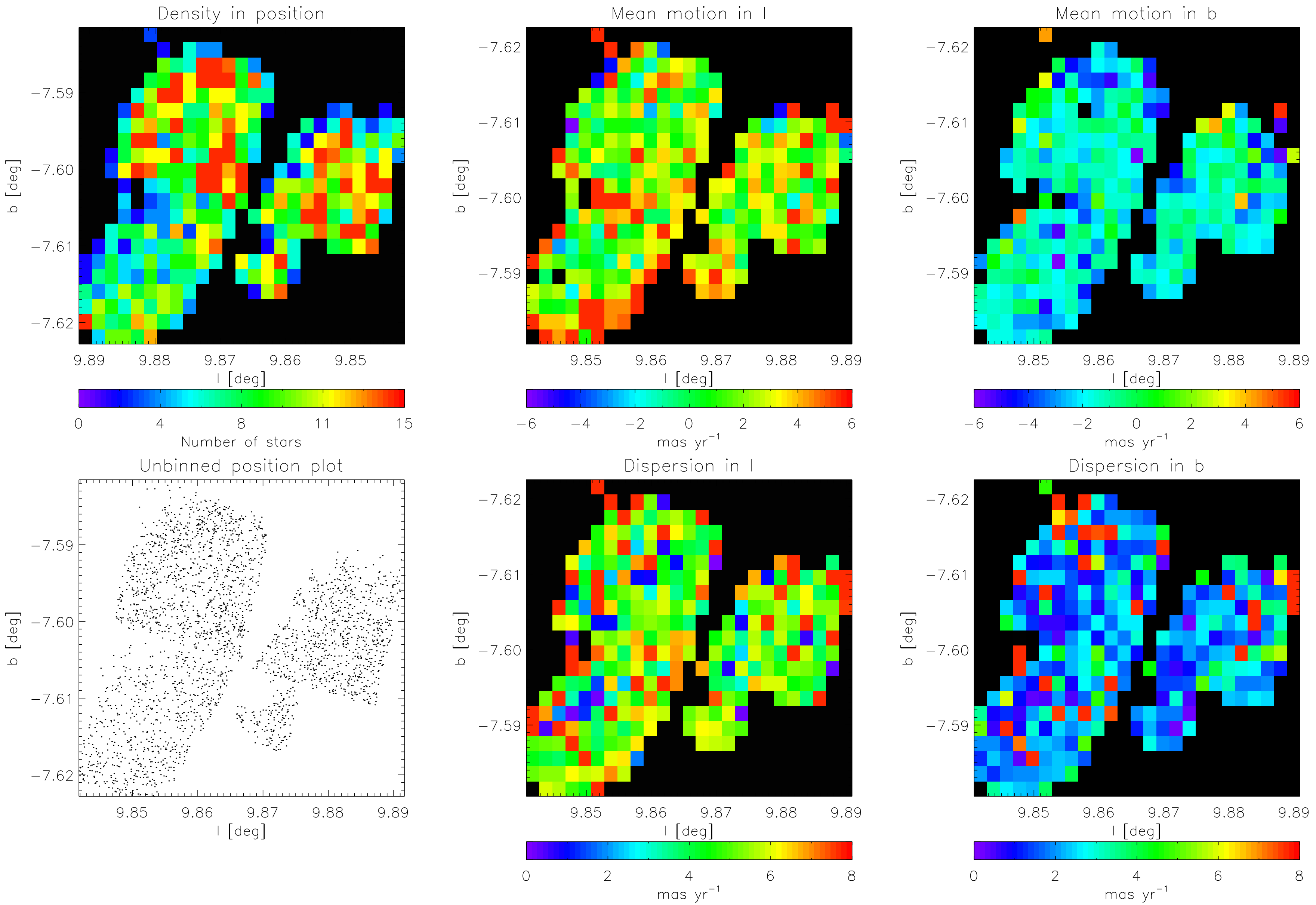

Figure 3.16: The tomography of Field 183635-235701. The sample is binned in 0.001 × 0.001 degrees box (corresponding to 3.6″ × 3.6″ box) and colour-coded in schemes according to the legend in the bottom of each plot. The scheme of the plot is the same as in Figure 3.15.

Chapter 4

Discussions and conclusions

We have conducted crowded-field photometry in Field 183635-235701, transform the resulting flight magnitudes into standard V and I system and correlate the resulting photometry catalogue with the already-measured proper motions catalogue. The resulting catalogue comprised of 2700 stars and contain positions, magnitudes in V and I band, as well as their proper motions.

Proper motions measurements are made by assuming that the mean motion of all stars in the field are zero in both components. However, the presence of cluster stars contaminating the field broke this assumption and traces of their motions are still present in the proper motion data, which appears in the form of a polynomial function of (x, y) position in the chip. By taking cluster stars as a reference point and setting their mean motion to zero, we manage to remove this residual and obtain a more accurate proper motions measurement.

The following is a discussion of the methods we employed and the results we obtained, divided into several sections.

4.1 Object detection

We used DAOPHOT to detect objects in the field, both for the photometry as well as the proper motions measurements. However, in both detection, a different set of model PSF was used. For the photometry, we chose several well-isolated stars in the chips to construct a model PSF. For the proper motion measurements, an analytic PSF model is used. This difference in methods of object detection results in different master list of object positions and both has to be correlated with each other. That is why there is a source-correlation procedure that resulted in—unfortunately—the loss of ~ 600 from the proper motions catalogue because we can not find matching stars within 3 pixels.

Population	c	$\bar{\mu}_l$	$\bar{\mu}_b$	σ_l	σ_b	θ
NGC 6656	264.12	-0.029	0.000	1.03	0.96	23.19
Bulge	17.47	10.945	- 4.013	2.30	-2.74	-31.97

Table 4.1: The parameters of the velocity ellipses for NGC 6656 and the bulge population, calculated by fitting a bivariate bimodal Gaussian function to the corrected proper motion data. We can compare the velocity dispersions before-and-after corrections were made by looking at Table 3.1.

Population	All chips	PC1	WF2	WF3	WF4
NGC 6656	1687	92	386	704	505
Bulge	710	51	212	250	197
cluster/bulge stars ratio	2.38	1.80	1.82	2.82	2.56

Table 4.2: The number of cluster stars and bulge stars, determined by counting the number of stars within 3σ of each velocity ellipse. The number of stars in each chips is also shown, as well as the ratio between the number of cluster and bulge stars found in each chip.

A better way to do the photometry and the proper motions measurements is to use the same master list for both process, once a definitive catalogue of object positions has been produced. This can bypass the source-correlation procedure altogether.

4.2 Bulge/Disk decomposition

Fitting the corrected proper motion distribution to a bivariate bimodal Gaussian function results in the parameters of the velocity ellipse for both population. The parameters for the velocity ellipse of both population is shown in Table 4.1. We use these parameters to separate the globular cluster and the bulge population within 3σ of the ellipse's major and minor axis. The result is shown in Figure 4.1(b) (with other alternatives of 1σ selection shown in 4.1(a)). We will use this 3σ cut for the following studies.

The number of cluster and bulge stars within 3σ of the respective velocity ellipse is shown in Table 4.2. In Figures 4.2 and 4.3 we plot the CMD of both population with respect of their position in the WFPC2 chip. Most of bulge stars lie in the WF3 chips, but that is also where the most number of cluster star lies. It is very hard, however, to ascertain in which chips the most stars of a certain population can be found, because there are empty areas in all four chips

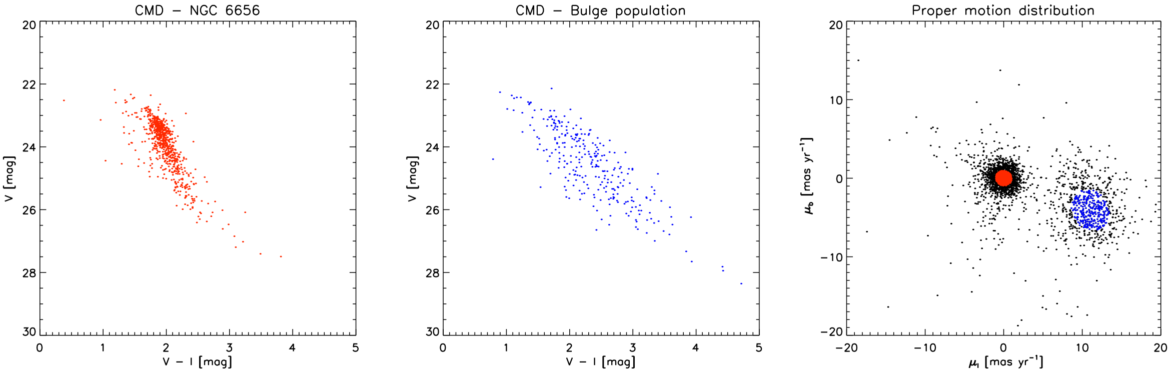

(a) 1σ velocity ellipse for both groups

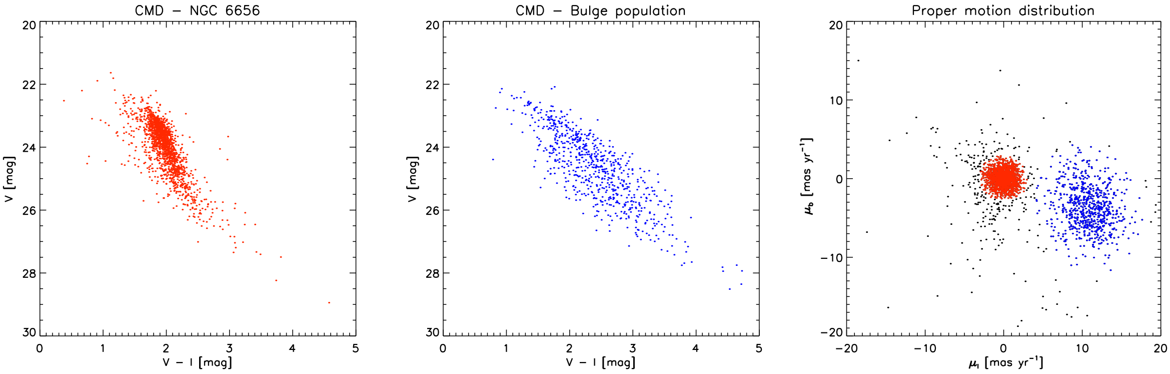

(b) 3σ velocity ellipse for both groups

Figure 4.1: The CMD for stars in NGC 6656 and members of the bulge population, selected by different criteria. 4.1(a) is made by drawing 1σ velocity ellipse in the corrected proper motion distribution, and 4.1(b) is by drawing a 3σ ellipse

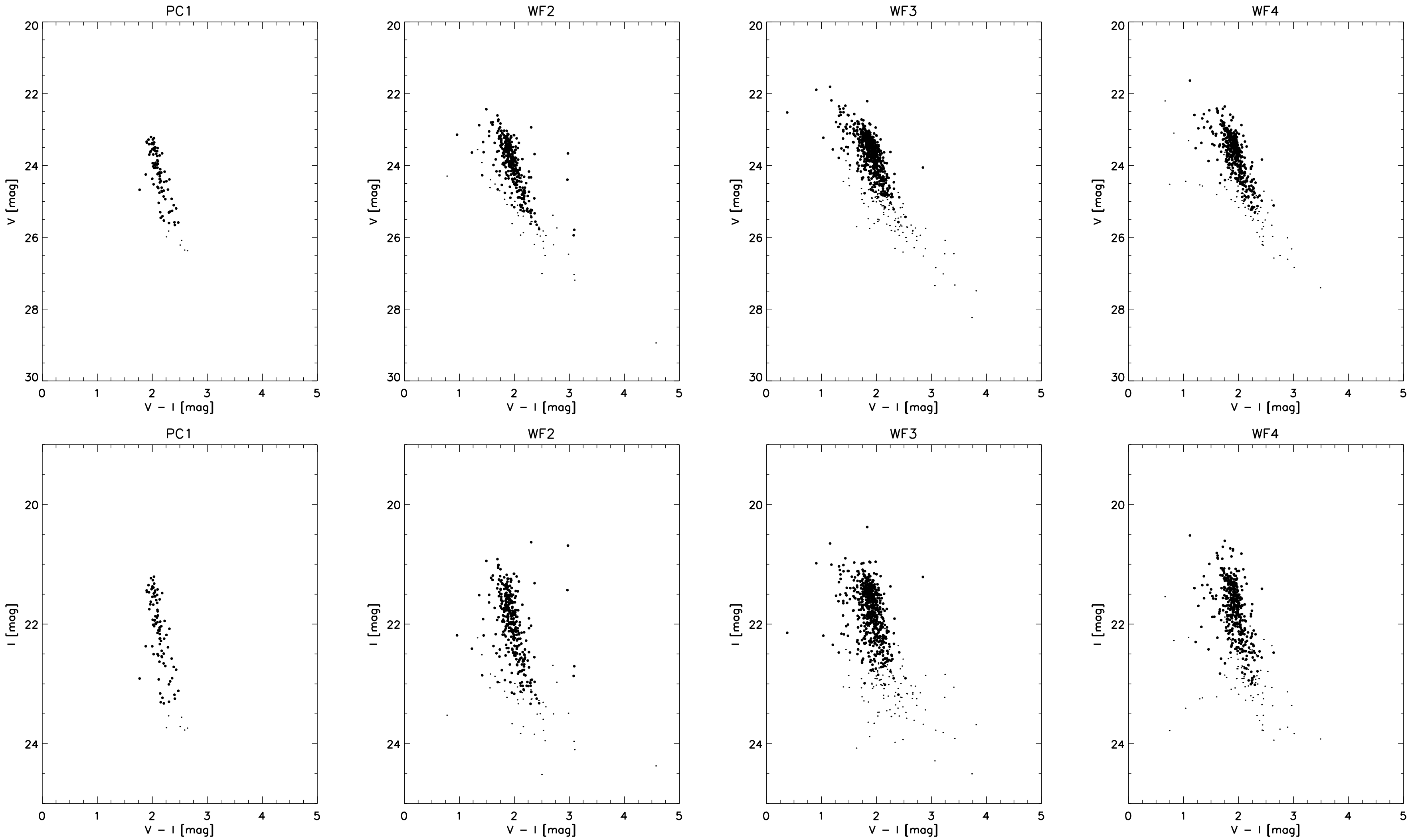

Figure 4.2: The CMD for 1687 cluster stars in Field 183635-235701, separated into each chips (from left to right): PC1, WF2, WF3, WF4. The selection of cluster stars are made by taking stars within 3σ of the velocity ellipse. The first row plot V magnitude against colour, while the second row plot I against colour. Heavier dots correspond to stars with errors better than or equal 0.1 mag.

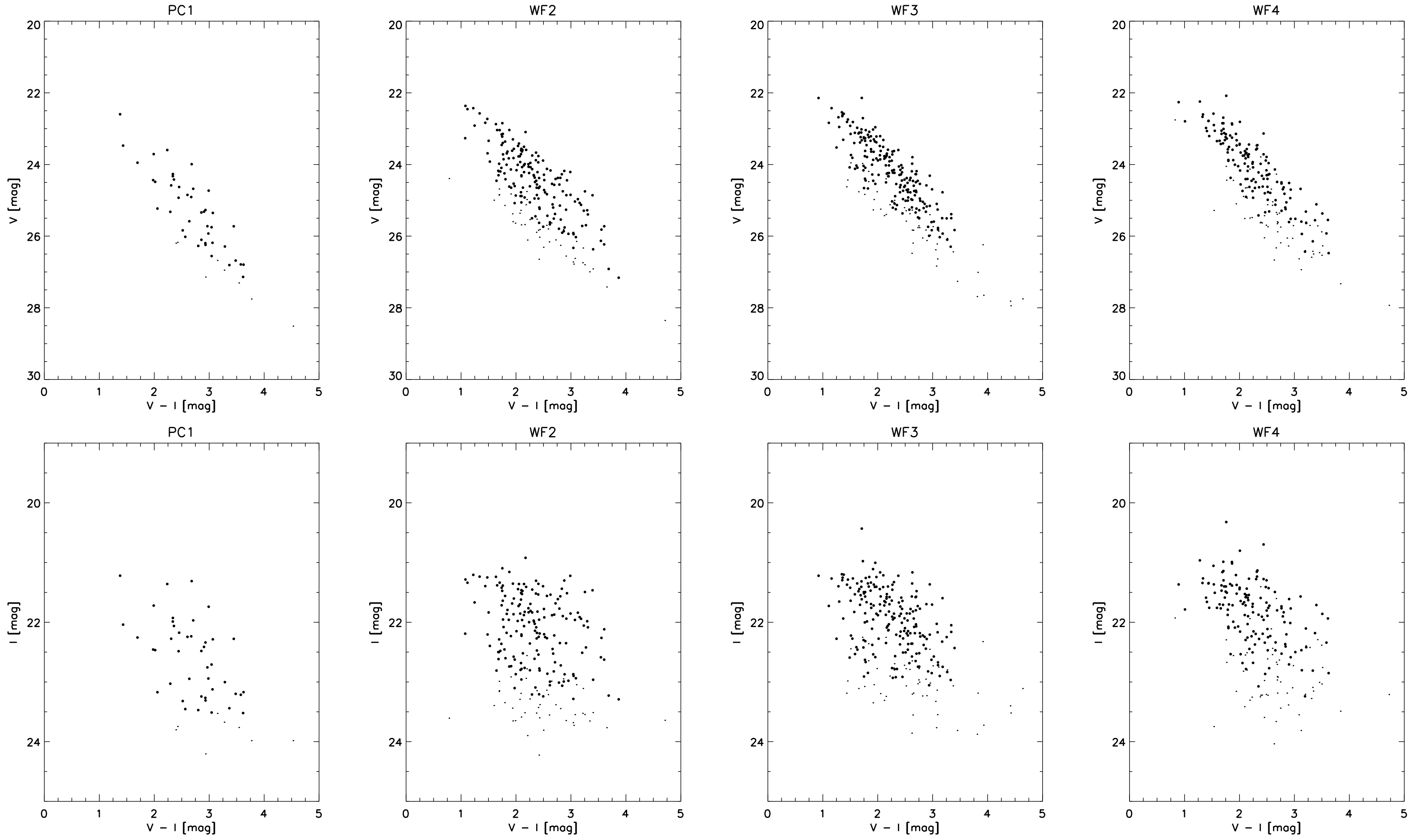

Figure 4.3: The same for Figure 4.2, but for 710 bulge stars in Field 183635-235701. Bulge stars are selected by taking stars within 3σ of the velocity ellipse.

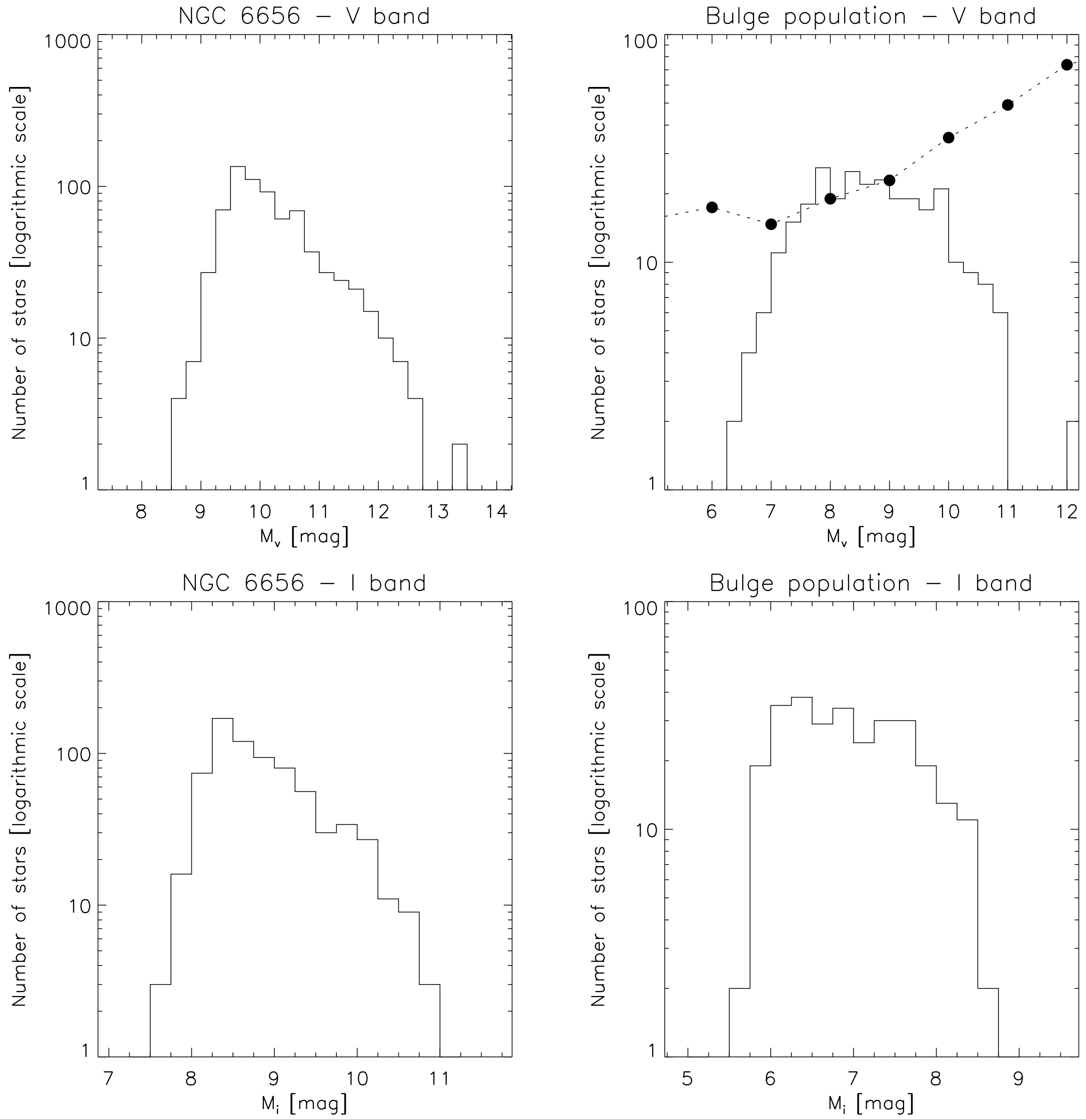

Figure 4.4: The absolute magnitude distribution of the cluster (left) and bulge population (right). The stars is selected according to the 3σ cuts. Absolute magnitude for cluster stars is estimated by adopting the intrinsic distance modulus of $(m - M)_0 = 12.56$ and colour excess $E(B - V) = 0.38$ (Monaco et al., 2004), while absolute magnitude for bulge stars is estimated by taking the distance to the bulge to be 8 kpc, corresponding to a distance modulus of ~ 14.52 and extinction $A_v = 1.28$ (Holtzman et al., 1998). The points in the bulge V luminosity function correspond to the luminosity function of the solar neighbourhood from Wielen et al. (1983).

(Figure 3.1. What we can say for sure at this point is that we found more stars (for both population) in the WF3 chips because that is the chip with the least empty area.

Because both cluster stars and bulge stars have more or less the same distance, their apparent magnitude reflects their luminosity. In Figure 4.4 we display the luminosity function of both populations. For cluster stars, we adopt the intrinsic distance modulus value of $(m-M)_0 = 12.56$ (corresponds to a distance of ~ 3.2 kpc) and colour excess of $E(B-V) = 0.38$ from the works of Monaco et al. (2004). We compare the luminosity function of cluster stars that we obtained with that of Piotto and Zoccali (1999), and conclude that due to saturation our data is badly undersampled for the bright-end of the magnitude distribution. The faint-end, however, shows a descending slope characteristic of a typical luminosity function of cluster population (Piotto and Zoccali, 1999). This is due to rapid decline in the luminosity of a main sequence star as its mass gets lower and approaches the limit for hydrogen burning at $M \approx 0.08 M_{\odot}$. Because we have decontaminate the cluster population from bulge stars, we might have actually obtain a more accurate luminosity function in the faint-end than what was obtained by Piotto and Zoccali (1999), in which they estimate the contamination to be $\sim 15\%$ at $V = 26.25$. The slope might also be caused by incompleteness in the faint-end. That is why we defer from estimating the peak of the distribution due to these incompletenesses in the bright-end and faint-end of the luminosity function. Complementary observations of stars in the bright-end of the luminosity function as well as deeper observation can complete the distribution and extend further the population study of this particular cluster.

The luminosity function for bulge stars is estimated by adopting a distance of 8 kpc to the bulge, corresponding to a distance modulus of ~ 14.52, and an extinction value of $A_V = 1.28$ (Holtzman et al., 1998). As a comparison, we also show the solar neighbourhood luminosity function in M_V from Wielen et al. (1983). The luminosity functions have been normalised so that they agree at $M_V = 9$. In the narrow range of $7 < M_V < 9$, it is apparent that the bulge luminosity function agrees with that of the solar neighbourhood. The bright-end fails to agree because of incompleteness due to saturation, while the faint-end does not conform because it close to the detection limit of the instrument. The agreement of the luminosity functions do not necessarily imply an agreement in the mass functions, however, because there might be observational errors and the different occurrences of binary between the two populations. A correct transformation to obtain the mass function is needed.

Investigator	(l, b)	σ_{V_l}	σ_{V_b}
Spaenhauer et al. (1992)	(1.02, -3.93)	115	100
Kuijken and Rich (2002)	(1.13, -3.76)	111	100
Kuijken and Rich (2002)	(1.25, -2.65)	123	108
Soto et al. (2007)	(1.13, -3.76)	116	106
This work	(9.86, -7.61)	85	109

all in km s^{-1}, assuming $R_0 = 8$ kpc

Table 4.3: The velocity dispersion in l and b direction compared to other works.

4.3 Kinematics of bulge stars

We use the stars within 3σ of the velocity ellipse for our analysis of bulge stars. Assuming a distance of 8 kpc to the bulge, we calculate the tangential velocity of bulge stars. The resulting velocity dispersions in l and b direction for bulge stars are shown in Table 4.3 and is also compared to previous works. The result fits well with previous findings that the velocity dispersion peaks at $l = 0$ and decreases toward positive and negative l (Figure 4.5).

The binned CMD for bulge stars is shown in Figure 4.6. Here the gradient of velocities in the mean μ_l that is so clearly present in Kuijken and Rich (2002) is barely discernible. For one given colour, the transition of velocities is not very clear. This might because we are not looking straight to the center of the bulge, but a bit off-axis, hence we have more contamination by inner disk stars.

We also calculate a crude distance estimator, in which we find that the quantity

$$M* = V - 1.5(V - I) \tag{4.1}$$

removes the slope of the main sequence of bulge stars in the CMD. This quantity can then be used as a relative distance indicator. In Figure 4.7 we plot the proper motions as a function of this distance modulus. In the l direction we see a gradient of rotation along the line sight. This can be due to contamination by disk stars or might reflect the true rotation of the bulge. This "rotation curve" does not look really pronounced like the one in Kuijken and Rich (2002), where the difference between the highest and the lowest point is ~ 4 mas yr^{-1}. Here the peak-to-peak difference is only ~ 1 mas yr^{-1}.

However, if this motion reflects the true rotation of the bulge, this crude "rotation curve" as well as the values of the velocity dispersion conforms well with the idea that the bulge rotates

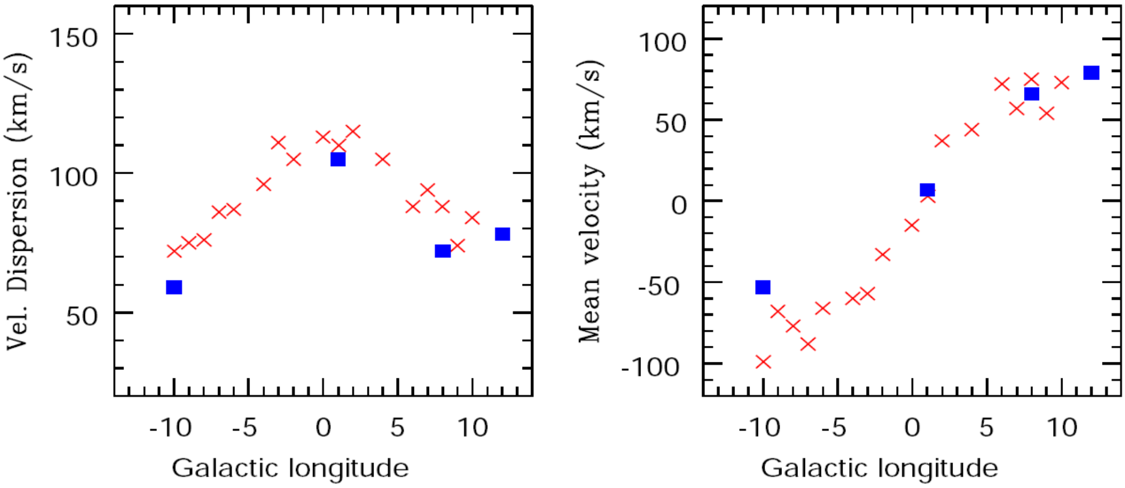

Figure 4.5: Velocity dispersion σ and mean velocity $\langle V \rangle$ as a function of Galactic longitude l. Crosses are recent data from Rich et al. (2007) and squares are data from Minniti (1996). Our data, $\sigma_{V_l} = 84$ km s^{-1} at $l = 9.86$ agrees well with these results. Source: Minniti and Zoccali (2008)

as a solid body.

4.4 Summary and Conclusions

Given a high enough precision on the photometry and the proper motion measurements, we have shown that it is possible to separate two different population solely by their kinematics. The assumption we made is that the bulge and the disc population exhibit different kinematics and this fact is pronounced on the velocity distribution. Our method of correcting for the residual motions due to contamination as well as separating the population by a bivariate bimodal Gaussian fitting works well and can be used to other “difficult” fields where there is high contamination by disc population. For our particular field, we can obtain an absolute reference frame not only by identifying extragalactic sources such as QSOs, but also by knowing the rest-frame velocity of the cluster contaminating our field (namely M22/NGC 6656). Future works should take advantage of this fact.

We manage to estimate the parameters of the velocity ellipse for both population and isolate 1687 cluster stars as well as 710 bulge stars. By studying only the “pure” bulge population, we calculate the luminosity function of both cluster and bulge stars, and obtain a better luminosity function for M22 that has less contamination. The resulting luminosity function for bulge stars is consistent with the luminosity function for the solar neighbourhood obtained by Wielen et al.

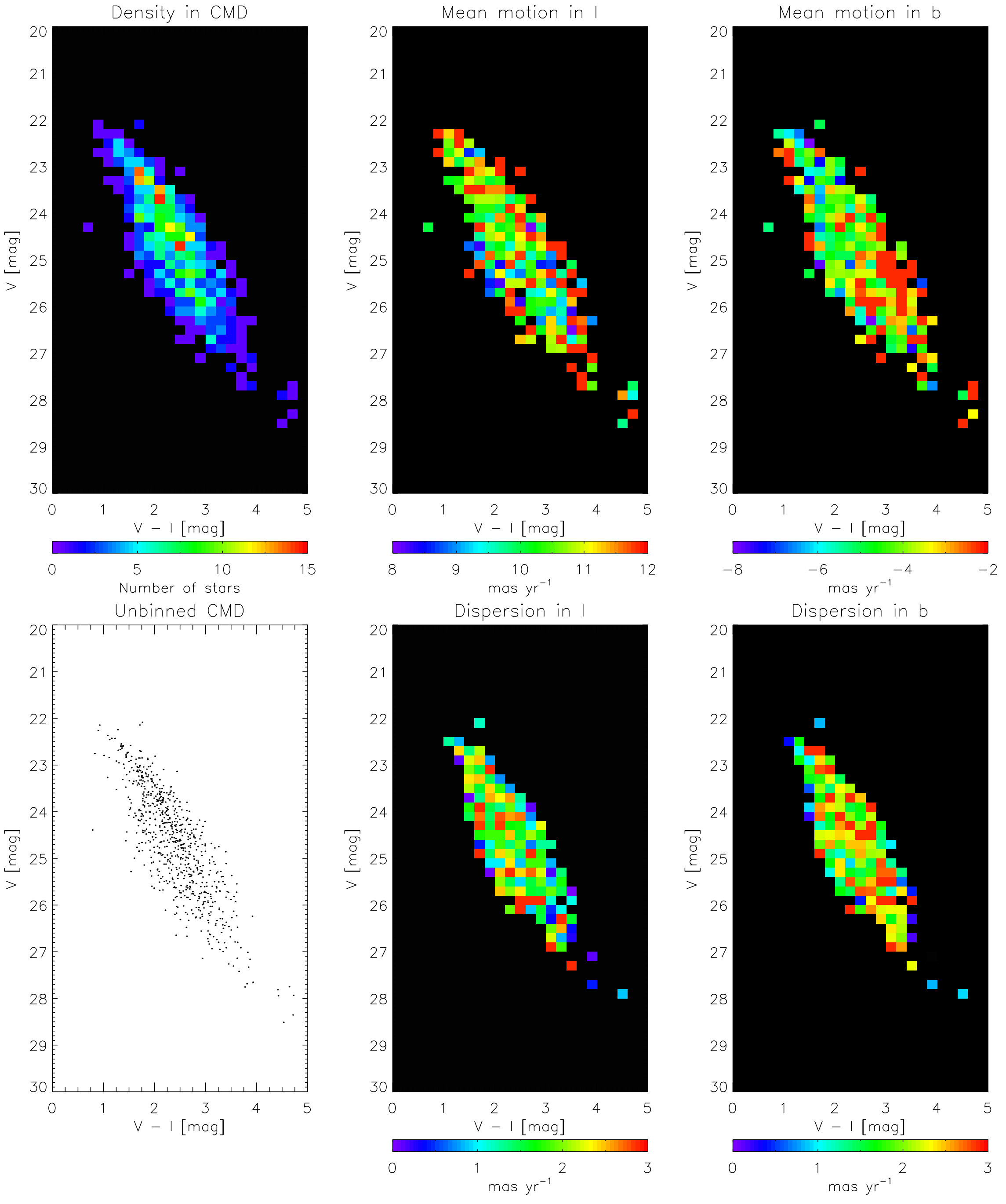

Figure 4.6: Same as in Figure 3.15, but for the bulge stars only, selected by drawing a 3σ velocity ellipse. The sample is binned in 0.2×0.2 mag box and colour-coded in schemes according to the legend in the bottom of each plot

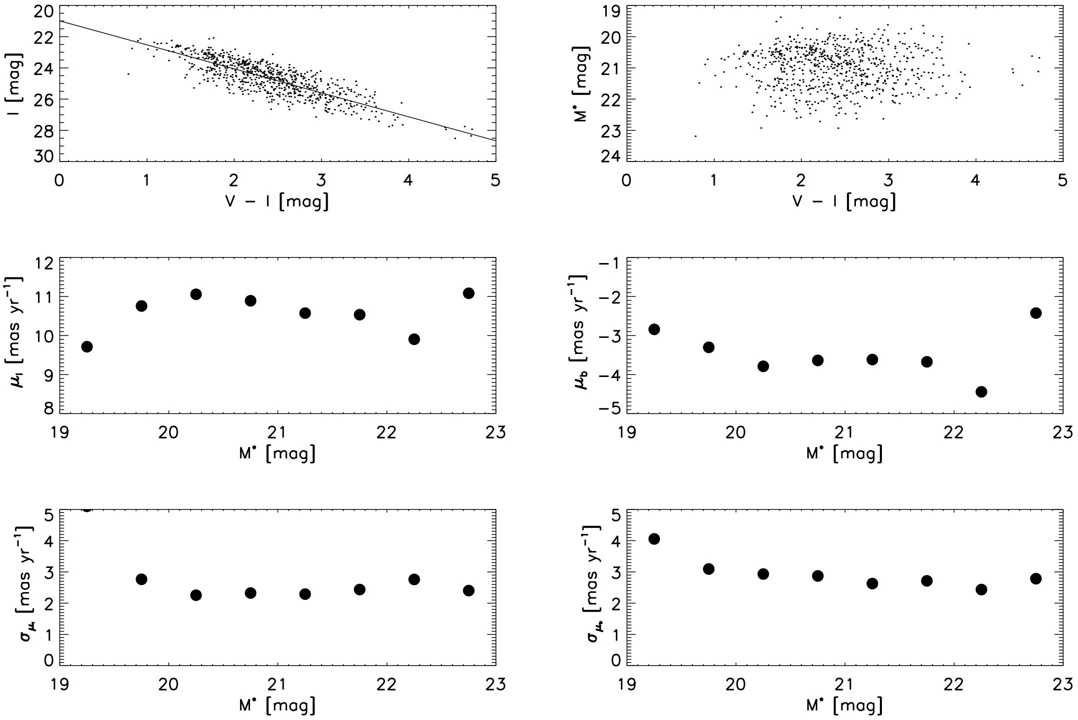

Figure 4.7: Proper motion statistics of the field against distance modulus $M*$. **Top left:** The CMD of bulge stars with the best-fit line of the main sequence; **top right:** The distance modulus is independent of colour; **Middle and bottom left:** Mean motion and dispersion in l plotted against distance modulus $M*$; **Middle and bottom right:** Mean motion and dispersion in b plotted against distance modulus $M*$.

(1983), albeit within a narrow magnitude. Future deep photometric observations of the bulge should be able to probe deeper and obtain a more accurate luminosity function.

Kinematical analysis of the pure bulge population yields values that are consistent with previous observations as well as contribute to the assertion that the bulge rotates as solid body. Further observations to obtain radial velocity data will reveal more about the properties of the Galactic bar and the triaxiality of the bulge. One of the things that can be done with a 3-D kinematics is to estimate the vertex deviation, and this can confirms current available models for the bulge, e.g Zhao (1996), Zhao et al. (1996).

Bibliography

Anderson, J. and King, I. R. 1999. *Astrometric and Photometric Corrections for the 34th Row Error in HST's WFPC2 Camera.* **PASP 111**: 1095–1098.

Binney, J. and Merrifield, M. 1998. *Galactic Astronomy.* Princeton, NJ : Princeton University Press (Princeton series in astrophysics).

Dolphin, A. E. 2000. *The Charge-Transfer Efficiency and Calibration of WFPC2.* **PASP 112**: 1397–1410.

Dwek, E., Arendt, R. G., Hauser, M. G., Kelsall, T., Lisse, C. M., Moseley, S. H., Silverberg, R. F., Sodroski, T. J., and Weiland, J. L. 1995. *Morphology, near-infrared luminosity, and mass of the Galactic bulge from COBE DIRBE observations.* **ApJ 445**: 716–730.

Eggen, O. J., Lynden-Bell, D., and Sandage, A. R. 1962. *Evidence from the motions of old stars that the Galaxy collapsed.* **ApJ 136**: 748–+.

Herschel, W. 1785. *On the Construction of the Heavens.* **Philosophical Transactions Series I 75**: 213–266.

Holtzman, J. A., Burrows, C. J., Casertano, S., Hester, J. J., Trauger, J. T., Watson, A. M., and Worthey, G. 1995. *The Photometric Performance and Calibration of WFPC2.* **PASP 107**: 1065–+.

Holtzman, J. A., Watson, A. M., Baum, W. A., Grillmair, C. J., Groth, E. J., Light, R. M., Lynds, R., and O'Neil, Jr., E. J. 1998. *The Luminosity Function and Initial Mass Function in the Galactic Bulge.* **AJ 115**: 1946–1957.

Hubble, E. P. 1922. *A general study of diffuse galactic nebulae.* **ApJ 56**: 162–199.

Ibata, R. A. and Gilmore, G. F. 1995. *The outer regions of the Galactic bulge - I. Observations.* **MNRAS 275**: 591–604.

Kapteyn, J. C. 1922. *First Attempt at a Theory of the Arrangement and Motion of the Sidereal System.* **ApJ 55**: 302–+.

Kuijken, K. 2004. *Stellar Kinematics of the Bulge from HST Proper Motion Measurements.* In Clemens, D., Shah, R., and Brainerd, T., editors, *Milky Way Surveys: The Structure and Evolution of our Galaxy* volume 317 of *Astronomical Society of the Pacific Conference Series* pages 310–+.

Kuijken, K. and Rich, R. M. 2002. *Hubble Space Telescope WFPC2 Proper Motions in Two Bulge Fields: Kinematics and Stellar Population of the Galactic Bulge.* **AJ 124**: 2054–2066.

Landolt, A. U. 1973. *UBV photoelectric sequences in the celestial equatorial Selected Areas 92-115.* **AJ 78**: 959–+.

Landolt, A. U. 1983. *UBVRI photometric standard stars around the celestial equator.* **AJ 88**: 439–460.

Lindblad, B. 1927. *On the state of motion in the galactic system.* **MNRAS 87**: 553–564.

Minniti, D. 1996. *Field Stars and Clusters of the Galactic Bulge: Implications for Galaxy Formation.* **ApJ 459**: 175–+.

Minniti, D., White, S. D. M., Olszewski, E. W., and Hill, J. M. 1992. *Rotation of the Galactic bulge.* **ApJ 393**: L47–L50.

Minniti, D. and Zoccali, M. 2008. *The Galactic bulge: a review.* In *IAU Symposium* volume 245 of *IAU Symposium* pages 323–332.

Monaco, L., Pancino, E., Ferraro, F. R., and Bellazzini, M. 2004. *Wide-field photometry of the Galactic globular cluster M22.* **MNRAS 349**: 1278–1290.

Oort, J. H. 1927. *Observational evidence confirming Lindblad's hypothesis of a rotation of the galactic system.* **Bull. Astron. Inst. Netherlands 3**: 275–+.

Oort, J. H. 1928. *Dynamics of the galactic system in the vicinity of the Sun.* **Bull. Astron. Inst. Netherlands 4**: 269–+.

Oort, J. H., Kerr, F. J., and Westerhout, G. 1958. *The galactic system as a spiral nebula (Council Note).* **MNRAS 118**: 379–+.

Piotto, G. and Zoccali, M. 1999. *HST luminosity functions of the globular clusters M10, M22, and M55. A comparison with other clusters.* **A&A 345**: 485–498.

Rich, R. M. 1988. *Spectroscopy and abundances of 88 K giants in Baade's Window.* **AJ 95**: 828–865.

Rich, R. M. 1990. *Kinematics and abundances of K giants in the nuclear bulge of the Galaxy.* **ApJ 362**: 604–619.

Rich, R. M., Reitzel, D. B., Howard, C. D., and Zhao, H. 2007. *The Bulge Radial Velocity Assay: Techniques and a Rotation Curve.* **ApJ 658**: L29–L32.

Sandage, A. and Bedke, J. 1994. *The Carnegie Atlas of Galaxies.* Washington, DC: Carnegie Institution of Washington with The Flintridge Foundation.

Searle, L. and Zinn, R. 1978. *Compositions of halo clusters and the formation of the galactic halo.* **ApJ 225**: 357–379.

Shapley, H. 1918a. *Globular Clusters and the Structure of the Galactic System.* **PASP 30**: 42–+.

Shapley, H. 1918b. *Studies based on the colors and magnitudes in stellar clusters. VII. The distances, distribution in space, and dimensions of 69 globular clusters.* **ApJ 48**: 154–181.

Shapley, H. 1919a. *Studies based on the colors and magnitudes in stellar clusters. XI. A comparison of the distances of various celestial objects.* **ApJ 49**: 249–265.

Shapley, H. 1919b. *Studies based on the colors and magnitudes in stellar clusters. XII. Remarks on the arrangement of the sidereal universe.* **ApJ 49**: 311–336.

Shapley, H. and Shapley, M. B. 1919. *Studies based on the colors and magnitudes in stellar clusters. XIV. Further remarks on the structure of the galactic system.* **ApJ 50**: 107–140.

Soto, M., Rich, R. M., and Kuijken, K. 2007. *Evidence of a Metal-rich Galactic Bar from the Vertex Deviation of the Velocity Ellipsoid.* **ApJ 665**: L31–L34.

Spaenhauer, A., Jones, B. F., and Whitford, A. E. 1992. *Proper motions of bulge stars.* **AJ 103**: 297–302.

Stebbins, J. and Whitford, A. E. 1947. *Six-Color Photometry of Stars. V. Infrared Radiation from the Region of the Galactic Center.* **ApJ 106**: 235–+.

Stetson, P. B. 1987. *DAOPHOT - A computer program for crowded-field stellar photometry.* **PASP 99**: 191–222.

Trumpler, R. J. and Weaver, H. F. 1953. *Statistical astronomy.* Dover Books on Astronomy and Space Topics, New York: Dover Publications, —c1953.

Whitmore, B. 1995. *Photometry with the WFPC2.* In Koratkar, A. P. and Leitherer, C., editors, *Calibrating Hubble Space Telescope. Post Servicing Mission* pages 269–+.

Wielen, R., Jahreiß, H., and Krüger, R. 1983. *The Determination of the Luminosity Function of Nearby Stars.* In Philip, A. G. D. and Upgren, A. R., editors, *IAU Colloq. 76: Nearby Stars and the Stellar Luminosity Function* pages 163–170.

Wyse, R. F. G., Gilmore, G., and Franx, M. 1997. *Galactic Bulges.* **ARA&A 35**: 637–675.

Zhao, H., Rich, R. M., and Spergel, D. N. 1996. *A consistent microlensing model for the Galactic bar.* **MNRAS 282**: 175–181.

Zhao, H., Spergel, D. N., and Rich, R. M. 1994. *Signatures of bulge triaxiality from kinematics in Baade's window.* **AJ 108**: 2154–2163.

Zhao, H. S. 1996. *A steady-state dynamical model for the COBE-detected Galactic bar.* **MNRAS 283**: 149–166.